Open access • Journal Article • DOI:10.1103/PHYSREV.170.1223

Nucleon Isobar Production in Proton-Proton Collisions between 3 and 7 GeV c

C. M. Ankenbrandt, Allan G Clark, Bruce Cork, T. Elioff ...+2 more authors

Institutions: University of California, Berkeley

Published on: 25 Jun 1968 - Physical Review (American Physical Society)

Topics: Production (computer science)

University of California

Ernest O. Lawrence Radiation Laboratory

NUCLEON ISOBAR PRODUCTION
IN PROTON-PROTON COLLISIONS BETWEEN 3 AND 7 GeV/v

C. M. Ankenbrandt, A. R. Clark, Bruce Cork,
T. Elioff, L. T. Kerth, and W. A. Wenzel

January 2, 1968

Berkeley, California

Submitted to Physical Review

UCRL-17763
Preprint

UNIVERSITY OF CALIFORNIA

Lawrence Radiation Laboratory
Berkeley, California

AEC Contract No. W-7405-eng-48

NUCLEON ISOBAR PRODUCTION IN PROTON-PROTON COLLISIONS BETWEEN 3 AND 7 GeV/c

C. M. Ankenbrandt, A. R. Clark, Bruce Cork,
T. Elioff, L. T. Kerth, and W. A. Wenzel

January 2, 1968

NUCLEON ISOBAR PRODUCTION IN PROTON-PROTON COLLISIONS BETWEEN 3 AND 7 GeV/c*

C. M. Ankenbrandt,† A. R. Clark, Bruce Cork,
T. Elioff, L. T. Kerth, and W. A. Wenzel

Lawrence Radiation Laboratory
University of California
Berkeley, California

January 2, 1968

ABSTRACT

A systematic study has been made of the reactions $pp \to pp$ and $pp \to pN^*$ in the angular range from $\theta_{lab} = 10$ deg to $\theta_{c.m.} = 90$ deg at 3, 4, 5, 6, and 7 GeV/c. An orthogonal dispersion magnetic spectrometer detected protons from interactions in hydrogen with momentum transfer (-t) in excess of 0.5 $(BeV/c)^2$. Well-defined peaks in the missing-mass spectra occurred at average N^* masses of 1240 ± 6, 1508 ± 2, and 1683 ± 3 MeV with average full widths of 102 ± 4, 92 ± 3, and 110 ± 4 MeV respectively. Below 2400 MeV no other significant enhancements were found. The N^* production cross sections $d\sigma/dt$ near $\theta_{c.m.} = 90$ deg are in qualitative agreement with the predictions of the statistical model. For each isobar the differential cross section at fixed energy varies as $\exp(-v/v_0)$, where $v \equiv [-tu/(t+u)]$; v_0 varies systematically with energy and tends toward the same value $[\approx 0.4\,(GeV)^2]$ for each isobar at the upper limit of our energy range.

I. INTRODUCTION

A good empirical description of N^* production at low momentum transfer in high energy proton-proton collisions,

$$pp \rightarrow pN^*, \qquad (1)$$

has emerged from recent experiments.[1-7] The main features of the data are the following:

(a) An enhancement near 1410 MeV has been observed at low momentum transfers.[3-7] This is usually interpreted as a P_{11} state ("Roper resonance"[8]) produced coherently, although some contribution may come from kinematic effects.

(b) The higher-mass resonances above 1688 MeV are not copiously produced at presently available energies.[1,2,4,6,7]

(c) The total production cross sections at high energy are roughly constant for the T = 1/2 isobars but fall with increasing energy for the T = 3/2 N^*(1238).[6] The N^*(1238) and N^*(1512) total production cross sections manifest peaks near their production thresholds.[7]

(d) The slopes of the differential production cross sections ($\frac{d\sigma}{dt}$ vs t) at low momentum transfer vary from about half to about twice that of the elastic cross section.[3,6,7]

Unlike the situation at low momentum transfers, the information on reaction (1) at medium and high momentum transfers [$-t \gtrsim 0.5$ $(GeV/c)^2$] has been confined to a few isolated data points.[2,5,6] The goal of the experiment reported here was a systematic survey of N^* production at relatively high momentum transfers.[9] The elastic scattering cross sections also were measured for comparison with N^* production and as a check on the experimental method.

The relative production cross sections for various isobars provide a direct test of the fundamental assumption of the statistical model, that final states are produced in proportion to their intrinsic statistical weights. As developed by Fast, Hagedorn, and Jones,[10, 11] the model has been applied with qualitative success to the description of pp elastic scattering at $\theta_{c.m.} \approx \pi/2$. Orear has suggested an empirical generalization to include center-of-mass angles different from $\pi/2$.[12, 13] He finds that a qualitatively useful fit to the data is given by

$$\frac{d\sigma}{d\Omega} = \frac{A}{s} \exp(-a\, p_\perp),$$

with $A = 595 \pm 135$ GeV^2 mb/sr and $1/a = 158 \pm 3$MeV/c, where

$$s = E^2_{c.m.} = 4(p^2 + M_p^{\,2}) \text{ and } p_\perp = p \sin\theta_{c.m.}.$$

However, this expression and the prediction of the statistical model are quantitatively inconsistent with recent precise p-p scattering data covering a wide range of incident momenta.[14-16] In fact, the elastic scattering cross section for $\theta_{c.m.} = \pi/2$ is fitted rather well by a phenomenological model[16] that uses a set of exponentials in $p_\perp^2$. The absence of "Ericson fluctuations" in elastic scattering also appears to contradict the predictions of the statistical model.[15]

Wu and Yang have given reasons for expecting that the high-energy dependence at fixed angle for a variety of cross sections may be similar.[17] Specifically they suggest that

$$\lim_{s\to\infty} \left[\ln \frac{d\sigma}{d\Omega}(\theta,\ pp \to pN^*) / \ln \frac{d\sigma}{d\Omega}(\theta,\ pp \to pp) \right] = 1. \quad (2)$$

It is important to note that this prediction, though consistent with that of the statistical model, is not dependent upon the specific nature of the interaction. Because of the logarithmic dependence in (2), it is unlikely that a very severe test is possible at the energies presently available.

II. EXPERIMENTAL METHOD AND APPARATUS

A. Introduction

The experiment employed the missing-mass method to measure N^* mass spectra indirectly. Application of the laws of conservation of energy and momentum to a reaction of the form

$$m_1 + m_2 \rightarrow m_3 + m_4,$$

involving particles or particle systems of invariant mass m_i, total energy E_i, and momentum $\underset{\sim}{p}_i$, yields the result

$$m_4^2 = E_4^2 - \underset{\sim}{p}_4^2 = (E_1 + E_2 - E_3)^2 - (\underset{\sim}{p}_1 + \underset{\sim}{p}_2 - \underset{\sim}{p}_3)^2.$$

In the laboratory system, in which particle 2, the target, is at rest, this reduces to

$$m_4^2 = m_1^2 - m_2^2 + m_3^2 + 2[p_1 p_3 \cos\theta_3 - (E_1 + m_2)(E_3 - m_2)],$$

where θ_3 is the lab angle between $\underset{\sim}{p}_1$ and $\underset{\sim}{p}_3$. Thus for a kinematically well-defined initial state, measurement of the momentum and angle of particle 3, together with a knowledge of its mass m_3, suffices to determine m_4, the "missing mass."

The orthogonal dispersion spectrometer used here has been described previously.[18] Through the use of a quadrupole lens and a vertical magnetic deflection, the spectrometer relates the production angle θ_3 and the momentum p_3 of a secondary proton to its horizontal and vertical displacements, respectively, in the focal plane. By the above equation, then, independent of horizontal source size, a given missing mass m_4 corresponds to a line in the focal plane; θ_3 and p_3 vary slightly along the line so as to keep m_4 constant. Hence a single hodoscope in the focal plane was used to measure the missing-mass spectrum. For this reason it was possible to use a small computer with a minimum of logic to accumulate the data required for the experiment.

B. Incident Beam and Target

Figure 1 is a schematic diagram of the beam. A liquid hydrogen target was located at the second focus of the external proton beam (EPB) of the Bevatron. The optics and geometry of the EPB have been described elsewhere.[19]

In the vertical plane the beam was imaged to a 0.2-in. spot at the target. Because the vertical position and spot size of the beam affect the measurement of the scattered momentum p_3, the position of the beam was checked periodically between runs by remotely viewing a scintillator that could be positioned behind the target. Because angular errors in the horizontal direction of the incident beam directly affect the measurement of the scattering angle θ_3, the horizontal angular spread of the beam at the target was limited to ± 0.5 mr through the use of quadrupole singlets in front of and behind the target. The direction of the beam was continuously monitored downstream from the target by left-right scintillators whose output was displayed on an oscilloscope in the electronics area. The horizontal width of the beam at the target was about 2 in.

The average beam intensity was of the order of 10^{11} protons per pulse, with a repetition rate of 11 pulses per minute. The spill length averaged about 500 msec during Bevatron "flat top" with little radio-frequency structure. The intensity was monitored by an ionization chamber located downstream from the target. The voltage induced on a capacitor by the collected charge was converted by an analog-to-digital converter and automatically recorded after each Bevatron pulse. In the early running at 7 GeV/c, the ion chamber was too far downstream; the greater beam width at this point adversely affected the reproducibility of the ion chamber readings. For this effect an error of ± 10% is applied to these early data.

It was essential that the beam momentum be held constant at a known value for each set of runs. This was accomplished by gating the scalers on when the Bevatron magnetic field fell between two preselected values. The field was measured by integrating the current induced in a current loop around the Bevatron by the changing magnetic field. The range of values accepted was usually ± 0.2%, matching the resolution in scattered momentum.

The liquid hydrogen—deuterium target was of conventional cryogenic design. The flask, approximately cylindrical but with rounded ends, was 4 in. in diameter and 12 in. long in the beam direction. It had sides of Mylar (0.0075 in.) and end domes of aluminum (0.0055 in. thick, 3.5 in. radius). The incident beam entered and left the vacuum jacket through windows of Mylar (0.020 in.) and aluminum (0.011 in.), respectively. The scattered secondaries exited through a total of 0.2 g/cm^2 of aluminum and Mylar.

C. Spectrometer Components

In Fig. 1, B_1 and B_2 are uniform-field "C" magnets which were movable to accept different laboratory-system production angles θ_3 between the limits of 10 and 70 deg. The magnet positions for these extreme angles are indicated in the figure. The movement of B_1 and B_2 was facilitated by use of air pads. Guide rails assured the proper relative alignment of the magnets. Bellows-type plastic bags, moving with the magnets, were filled with helium to reduce the scattering along the beam path.

The remainder of the magnets defined a fixed channel at an angle of 14 deg to the incident beam. When necessary a concrete block was moved into position behind B_2 to shield the fixed channel from particles coming directly from the target. A vacuum pipe occupied the fixed portion of the beam path, from B_3 through B_6. B_3 directed the scattered particles down the fixed channel. Magnets B_4, B_5, and B_6 were identical "H" magnets which produced a total vertical deflection of 15 deg for a central-momentum particle. All the bending magnets were shimmed to provide magnetic field path integrals uniform to 0.1% over their apertures.

Q_1 and Q_2 constituted a quadrupole doublet with a 7.75-in.-diameter aperture; Q_1 focused the beam horizontally and Q_2 focused vertically. In the horizontal plane, particles produced at a given angle θ_3 from any point on the target were focused to a point in the image plane. Vertically the beam spot at the target was focused at the image plane.

The Cerenkov and scintillation counter detection system was located in or near the image plane. The heart of the detection system was a 28-counter scintillator hodoscope in a plane perpendicular to the spectrometer axis at the image plane. Each element was viewed by a 1P21 photomultiplier and had a sensitive area of 6.75 by 0.25 in. and thickness of 0.5 in. in the beam direction. The entire hodoscope could be rotated around the spectrometer axis by remote control to align the elements with lines of constant missing mass.

D. Spectrometer Optics

The beam-optical properties of the spectrometer are illustrated by the ray diagrams of Fig. 2. In the approximation that chromatic aberration and vertical source size are neglected, the momentum and angle of a scattered particle are uniquely determined by the coordinates of its intersection with the hodoscope.

In the vertical plane, an image of the beam spot at the target is produced at the hodoscope. If the spot size is neglected, the vertical coordinate depends only on the momentum of the particle. For small deviations of the momentum p_3 from its value p_c at the center of the hodoscope, we may write

$$y = D \frac{\Delta p}{p_c} \qquad (3)$$

in the Cartesian coordinate system defined in Fig. 2, where D (= 59.2 in.) is the dispersion at the hodoscope and $\Delta p = p_3 - p_c$.

In the horizontal plane θ_h represents the projected angle between the incident beam direction and the trajectory of a particle as it enters the quadrupole. Because the hodoscope lies at the horizontal focus of the optical system, the horizontal displacement at the hodoscope is given by

$$x = f_h \Delta\theta_h, \tag{4}$$

where f_h is the horizontal focal length and $\Delta\theta_h$ is the deviation of the trajectory from the central ray of angle θ_{hc}. The focal length f_h is 612 in. when $\theta_3 = \theta_{hc} = 14$ deg, and depends only slightly on θ_3.

The variations in p_3 and θ_3 over the hodoscope are small; therefore the missing mass is essentially constant along a line of slope m, where

$$m = \left(\frac{\partial y}{\partial x}\right)_{M_4} \equiv -\tan\delta;$$

δ is the angle of rotation required for the hodoscope in order that each counter detect the smallest range of missing masses.

Using Eqs. (3) and (4) and letting Φ_1 and Φ_2 be the angles of deflection in B_1 (or B_2) and B_3 respectively, we find that

$$\cot\delta = \frac{f_h}{D}\left[2\Phi_1 + \Phi_2 - p_3\left(\frac{\partial\theta_3}{\partial p_3}\right)_{M_4}\right].$$

The range of masses $\Delta(M_4^{\,2})$ that a single hodoscope element accepts is determined by the rate of change of missing mass in the direction normal to that element. Explicitly we find

$$\Delta(M_4^{\,2}) = 2p_1\, p_3\, (w/f_h) \sin\theta_3 \csc\delta$$

for a detector of width w. For the conditions of this experiment, ΔM_4 is typically about 10 to 20 MeV.

F. Particle Detection and Fast Electronics

The particle identification system for this experiment consisted of a scintillator and Cerenkov counter telescope to select particles of the desired type in the scattered beam. The good resolving time of the counter system and the location of these detectors far from the target enables us to use high intensity in the EPB to obtain good data rates.

For detecting protons, as required for the present experiment, the Cerenkov counters were not needed because π^+ and K^+ contaminations were small. When not in use, the Cerenkov counters could be lowered out of the scattered beam. Two scintillators S_2 and S_3 were placed in coincidence with the hodoscope. S_3 defined a 6.75-in. effective length for each hodoscope element; S_2 was slightly larger. Anticoincidence counter A reduced background in the hodoscope light pipes. The orientation of these scintillators is shown in Fig. 3.

With time resolution ≈ 20 nsec, master coincidence $E \equiv S_2 S_3 \overline{A}$ and secondary coincidences $h_i \equiv EH_i$ for each hodoscope counter H_i were recorded on scalers of six and three decades respectively. An additional six-decade scaler E' summed h_i, but provided only a single count in a case of coincidence within the electronic resolving time. Comparison of E and E' therefore provided a direct test for accidental hodoscope coincidences or multiprong interactions in the scattered beam.

G. Data Acquisition and Storage

The rapid rate of data accumulation necessitated use of a small computer (the Digital Equipment Corporation PDP-5), both to facilitate data storage and to monitor the progress of the experiment and the performance of the equipment.

The experiment was divided into runs according to the settings of the variable parameters of the apparatus. For the experiment described here the duration of a run was typically a few minutes. At the start of each run the position of the movable magnets and the magnet currents for $B_4B_5B_6$ were read into the computer via an analog-to-digital converter. After each Bevatron pulse, the computer read and reset 30 scalers (H_{1-28}, E, and E') and the integrator for the ion chamber. The information from each accelerator pulse was written on magnetic tape, then added to the previous data stored in the computer. The limit of 10^3 per pulse on the hodoscope scalers occasionally led to overflow problems, particularly at the elastic peak, where the incident beam intensity often had to be decreased. In a typical case of overflow, only the most significant digit was lost. Because the data for each pulse were recorded spearately, occasional overflows could later be identified and either corrected or eliminated by comparing the sum of the hodoscope counts with the E and E' counts or by checking the smoothness of the data.

A display oscilloscope provided the main on-line feedback of data to the experimenters. For example, histograms of the hodoscope data, either cumulative or pulse-by-pulse, could be displayed. In this way an almost continuous record of the progress of a run was available. At the end of a run a Polaroid photograph of the cumulative spectrum was usually made, and the accumulated data were typed on a teletype and written on magnetic tape.

III. ANALYSIS OF THE DATA

A. Analysis of Individual Runs

1. Differential Cross Section

The basic results of this experiment are missing-mass spectra for various fixed incident momenta and lab angles. These spectra take the form of double differential cross sections ($d^2\delta/dM_4{}^2dt$) as functions of p_1, θ_3, and M_4. The cross sections are given in terms of experimentally determined quantities by the formula

$$\frac{d^2\sigma}{dM_4{}^2dt}\ (p_1,\ \theta_3,\ M_4) = \frac{N_s}{N_i n_t}\ \frac{1}{\Delta\Omega_L\Delta M_4{}^2}\ J\left(\frac{M_4{}^2,\ \Omega_L}{M_4{}^2,\ t}\right), \qquad (5)$$

where N_s = number of protons scattered into lab solid angle $\Delta\Omega_L$ with squared missing mass in the range $\Delta M_4{}^2$,

N_i = number of incident protons,

n_t = target thickness in protons per unit area,

$J\left(\frac{M_4{}^2,\ \Omega_L}{M_4{}^2,\ t}\right)$ = Jacobian transformation from lab solid angle Ω_L to invariant four-momentum transfer squared, t,

$= \pi\ [(E_1 + M_2)\ \beta_3 - p_1 \cos\theta_3]/(M_2\, p_1\, p_3\, \beta_3)$.

This section describes the analysis and corrections necessary to deduce these cross sections from the raw data via Eq. (5).

2. Combination of Data into Runs

For each run the data from different Bevatron pulses were combined. These data consisted of 30 scaler readings (H_{1-28}, E, E') and the voltage V proportional to the integrated beam intensity

($0 \leq V \leq 10$ volts). In combining the data pulse-to-pulse consistency was checked. Data from a pulse were eliminated if they contained an unrecoverable scaler overflow, if they were obviously inconsistent with those from the other pulses, or if V was outside the range 0.5 volt $\leq V \leq$ 9.5 volts. Each of these requirements eliminated about 5% of the data. The combined data yielded N_s (Eq. 5) for a set of 28 adjacent mass intervals. N_i was determined from the ion chamber calibration.

3. Kinematics

For each hodoscope element, the kinematic quantities that enter Eq. (5) are completely determined by the optical properties of the spectrometer. In preparation for the experiment the kinematic quantities and the corresponding spectrometer settings (magnet currents, angle δ, and movable magnet position) were calculated for sets of runs at constant p_1 and θ_3. Each set covered overlapping intervals in M_4 to define a complete missing-mass spectrum. Included in each set were runs centered at 938, 1238, 1512, and 1688 MeV, the nominal locations of elastic and isobar peaks.

During the course of the experiment, systematic errors in the positions of elastic peaks were observed. Careful measurement of the spectrometer geometry and the magnetic field integral through $B_4B_5B_6$ indicated slight (< 1%) deviations from nominal values. In addition there were errors of the order of 1% in calculating p_1 from the integrated Bevatron field, errors of the same order in determining p_3 at the center of the hodoscope, and uncertainties of the order of a few mr in determining θ_3 from the channel angle θ_h and the horizontal bending angles.

After all the measured corrections to the spectrometer geometry and magnet excitation curves were applied, there remained systematic errors of about ± 50 MeV in the missing-mass measurements for pp elastic scattering and for $pp \rightarrow \pi^+ d$. Hence the momentum scale P_3, the incident beam direction ($\theta_3 = 0$), and (separately for each incident energy) the value of P_1 were adjusted to provide best agreement with the known kinematics for these two final states. Approximately 75 measurements were used in this adjustment. In this way the uncertainty in the mass scale was reduced to about ± 5 MeV.

4. Laboratory-System Solid Angle

The calculation of the laboratory-system solid angle subtended by each hodoscope element used well-known matrix methods of ray tracing.[20] The matrix representations of the optical elements (magnets and drift spaces) were adapted from those used by Devlin.[21] In this method the components of a ray vector $x = (x, x', y, y', \Delta p/p)$ are the deviations of the ray in position, direction, and momentum from the central ray. The computer program determined $\Delta y'_T$, the acceptance interval of vertical directions y'_T at the target, for a set of rays equally spaced in x_T, x'_T, and Δp. For a given run, the solid angle calculation, which included determination for $\Delta y'_T$ for about 1000 combinations of x_T, x'_T, and $\Delta p/p$ and integration over 28 hodoscope elements, required about 6 seconds of CDC 6600 computer time.

The solid angle was typically about 10^{-4} steradian. The "illumination" on the hodoscope was almost uniform vertically but decreased by about a factor of two from center to edge horizontally. Thus the solid angle was about the same for each hodoscope element unless the angle δ was large.

5. Counting Corrections

The following three effects were sources of background in the observed proton spectra:

a. Counts in two or more hodoscope elements caused by a single secondary particle ("double counts").

The presence of a significant number of double counts in our apparatus was indicated empirically by the fact that the sum of the hodoscope counts consistently exceeded the number in E' by about 8%. This excess was a measure of the number of times two or more hodoscope counts occurred within the resolving time of the E' circuitry. That accidental coincidences between two scattered beam particles did not account for a significant part of this excess was indicated by direct estimates of the accidental rate and was verified by the fact that the excess was approximately independent of the scattered beam flux. In fact, estimates indicate that the following effects account for most of the excess: passage of a single particle through two hodoscope elements ($\approx$ 0.5%), interactions of scattered-beam particles in S_2 and in the hodoscope ($\approx$ 2%), and production of δ rays in S_2 and in the hodoscope ($\approx$ 4%). These effects usually produced spurious counts close to the original particle path, thereby preserving the shape of the spectrum; hence the required correction involved simply a renormalization and was made by dividing each hodoscope count by the observed ratio of ΣH_i to E' for each run.

b. Interactions in windows and walls of the hydrogen target.

The counting rate with target empty was found to be about 5%

of the full-target rate for a representative small sample of runs. Since this background was caused almost entirely by scattering from composite nuclei, it did not show the structure inherent in the secondary spectra from proton-proton interactions. Therefore, after the spectra observed with target full had been fitted to a background function plus peaks, a correction was made by subtracting from the data 5% of the value given by the background function.

c. Secondaries other than protons.

The background from particles other than protons has been neglected in the analysis of the data because its effect is small compared with the other corrections and because it contributes a smooth background (except for the small and readily identified peak from $pp \rightarrow \pi^+ d$). The proton spectra of interest lie near the kinematic limits of pion and kaon production, so that these are either kinematically impossible or strongly suppressed by the small phase space available. A few direct measurements of pion yields confirmed that this background was small enough to be neglected.

B. Analysis of Elastic Data

The missing-mass spectrum of Fig. 4 shows typical data in the elastic scattering region in order to obtain the elastic scattering cross section and at the same time to evaluate the resolution of the spectrometer, it is assumed that the true peak intensity distribution for elastic scattering is a Gaussian in M_4, centered at M_0 and of width Γ. The background is represented by a polynomial. This function is fitted to the measured data by a least-squares fitting program with M_0, Γ, the Gaussian amplitude A, and the polynomial coefficients as variable parameters. The order of the polynomial is adjusted to obtain the best fit. Then Γ is the observed resolution at the elastic peak, and the number of elastically scattered protons is obtained by subtracting the polynomial from the data in the neighborhood of the peak.

The differential cross sections for proton-proton elastic scattering from this experiment are presented in Fig. 5 and Table I. The uncertainties given are compounded from statistical errors, uncertainties resulting from random errors in the kinematic variables (including t), and, when applicable at 7 GeV/c, random errors of 10% in the incident beam intensity (see Section II B). The errors given do not include an estimated error of 7% in the absolute normalization.

In Fig. 6 our elastic cross sections at 3, 5, and 7 GeV/c are compared with the results of Clyde et al.[14] at corresponding momenta. The agreement is reasonably good; differences may be attributed primarily to absolute calibration errors, which are somewhat larger in the experiment described here. Quantitative interpretation of our elastic cross sections is postponed to Section V for comparison with the inelastic results.

C. Combination of Inelastic Runs into Composite Mass Spectra

After the analysis of individual runs described in Section III A, the inelastic data were combined into composite missing-mass spectra at constant p_1 and θ_3. There was usually considerable overlapping of adjacent runs, which provided another self-consistency check.

It was found that the data from the ends of the hodoscope were consistently in error, presumably because of small errors in aperture location, nonuniform distribution of background on the hodoscope, and similar effects; for this reason data from hodoscope elements 1 through 4 (at the top of the hodoscope) and from element 28 have been rejected.

In order to obtain the mass spectra at constant angle, additional corrections to the data are needed to compensate for the variation in lab angle across the hodoscope for each run and to allow for slight changes in the corrected central θ_3 from run to run. Although the variations are small, they contribute a significant effect because of the strong dependence of the cross section on θ_3. Correction for this effect was made empirically by using the observed angular dependence of the counting rates at fixed p_1 and M_4; the necessary geometrical factors were evaluated as a "by-product" of the program for calculating solid angles. The resulting correction is greatest at smallest angles; the largest correction required was 18%. The uncertainty in the correction is estimated to be ± 20% of its magnitude. In a few cases, systematic differences between adjacent runs have not been completely removed by the corrections. This is apparent in the data of Figs. 7 through 12.

IV. RESULTS

A. Mass Spectra

The mass spectra of Fig. 7 show a lack of pronounced structure beyond the peak near 1688 MeV. On the basis of these data we confined the remainder of the experiment to the missing mass region below about 2000 MeV.

The missing mass spectra measured at 3, 4, 5, 6, and 7 GeV/c are presented in Figs. 8 through 12, respectively. The data of Fig. 7 with missing masses below 2000 MeV are repeated for comparison with the other spectra. Note that data taken at 7.0 and at 7.1 GeV/c are combined in Fig. 12. The errors shown include statistical errors, which are usually about 1%, and the effect of the uncertainty in the scattering angle θ_3. The solid curve associated with each spectrum is the nonresonant background as estimated by the fitting procedure to be described in Section IV C.

The enhancements near 1512 and 1688 MeV are strongly excited at all our angles for all incident momenta except 3 GeV/c. The 1238-MeV peak, on the other hand, decreases rapidly as either the incident energy or the momentum transfer increases. We find no evidence for the enhancement near 1410 MeV which has been observed at lower momentum transfers.[3-7] Finally, at 3 GeV/c we see the enhancement near the inelastic kinematic limit ($M_4 \approx 1100$ MeV) that has been attributed[2,7] to detection of the decay protons from $N^*(1238)$ isobars produced with nucleons.

B. Breit-Wigner Fits

To obtain a quantitative measure of the nucleon isobar effects in our data, we made least-squares fits to the spectra, using a sum of Breit-Wigner resonant forms plus a polynomial representing the nonresonant background:

$$\frac{d^2\delta}{dM_4^2 dt}(M_4) = P(M_4) + \sum \frac{H_i}{(M_i - M_4)^2 + (\Gamma_i/2)^2}. \qquad (6)$$

In this equation, H_i, M_i, Γ_i, and the coefficients of the polynomial $P(M_4)$ are variable parameters; the sum extends over the peaks near 1238, 1512, and 1688 MeV provided that such peaks are apparent in the data. For each spectrum the order of the polynomial was increased until a satisfactory fit was obtained; in particular, that fit was chosen for which no further significant improvement in χ^2 was obtained by increasing the order of the polynomial. From these fits were obtained sets of parameters--mass M, full width Γ, and height H--to characterize each peak. The quantitative study of N^* production is made in terms of these parameters.

A search was made for dependence of the mass and width of each isobar peak on the incident energy or the momentum transfer or both. Shifts could arise from differences in the dynamics of the production and decay of a resonance or from the superposition of more than one resonance in any peak. After our resolution was unfolded, no significant dependence of mass or width on the kinematics was found. Hence for each isobar a best value of mass and width was found by averaging all the independently determined values. For the $N^*(1238)$, a correction of 23 MeV, as estimated by Jackson,[22] was applied for the well-known fact that the peak does not occur at the true mass of the resonance. The average masses and widths are given in Table II.

The position of each peak on the missing-mass scale is very well determined (about ± 3 MeV) by the fitting procedure; the dominant uncertainty in mass arises from random errors in the mass scale itself. These errors were estimated from the spread in the proton and deuteron mass determinations (see Section III A) and are in a sense checked by the self-consistency of the mass determinations from the various spectra. For the 1238-MeV enhancement an additional uncertainty of ± 5 MeV in the "Jackson correction" is assumed.

Unlike the mass at a peak, the width is not determined precisely by the fitting procedure. The reason is that the polynomial background is too "accommodating": a decrease in the background in conjunction with an increase in the height (and simultaneously the width) of a peak does not greatly affect the goodness of fit. The errors in the widths as estimated by the fitting procedure are typically about 15 MeV. These errors are compounded with the estimated uncertainty in unfolding our resolution before forming the weighted averages of Table II.

C. Differential Cross Sections for N^* Production

The large and correlated errors in the height and width of a peak would lead to great uncertainties in calculating the production cross sections (proportional to height times width) from the Breit-Wigner parameters. Therefore, using Eq. (6), we made additional fits in which the isobar widths were fixed at the average values given in Table II. With this procedure the uncertainty in the background polynomial was considerably reduced.

The N^* production cross sections were determined from the area under the corresponding peaks, evaluated from the Breit-Wigner parameters of the fixed-width fits. The errors were propagated from the error matrix of the parameters, a procedure that takes into account the uncertainties in background subtraction. The values for 7.0 and 7.1 GeV/c include an additional uncertainty arising from the random errors in measuring the incident beam intensity, as described in Section II B.

Systematic errors in the absolute normalization are not included. It is estimated that systematic errors in measuring the incident beam intensity and in calculating the solid angle contribute a ± 7% uncertainty and that errors in the average widths used in our fitting procedure (see Table II) contribute an additional ± 10% uncertainty in absolute normalization.

The cross sections are presented in Tables III, IV, and V and in Fig. 13. The data of Blair et al.[7] at lower momentum transfers and comparable energies are represented by the solid lines in Fig. 13.

Some general features of the cross sections at medium and high momentum transfers are the following. The cross sections for all isobars, like the elastic cross section, decrease rapidly with energy. For the isospin 1/2 states $N^*(1512)$ and $N^*(1688)$ the production cross sections show similar behavior: both are slowly varying as functions of momentum transfer; at 90 deg c.m. they are significantly larger than the elastic cross section. The cross section for the 1238-MeV resonance, like the elastic cross section, falls more steeply with momentum transfer.

V. DISCUSSION OF RESULTS

Hagedorn has extended the statistical treatment of proton-proton elastic scattering to arbitrary two-body processes pp → AB near $\theta_{c.m.}$ = 90 deg at high energy.[11] For $pp \rightarrow pN^*$ he makes the prediction

$$\frac{d\sigma}{dt}_{pp \rightarrow pN^*} = \left[\alpha^2 \left(\frac{2J_{N^*} + 1}{2}\right) \frac{K_{pN^*}}{K_{pp}} \; \frac{\rho_{pN^*}}{\rho_{pp}}\right] \left(\frac{d\sigma}{dt}\right)_{pp\ \mathrm{elastic}}, \quad (7)$$

where α is the Clebsch-Gordan coefficient for projecting the final pN^* isospin state on the pure I = 1 initial state, J_{N^*} is the isobar spin, K_{pN^*} is a kinematical factor involving center-of-mass quantities in the final state, and ρ_{pN^*} is two-body phase space for the pN^* final state. There are no adjustable parameters in Eq. (7).

In comparing the predictions of (7) with our measurements, we have used the measured elastic cross sections (Figs. 5 and 6) rather than those predicted from the statistical model;[11] and we have assumed that the observed peaks at 1512 and 1688 MeV are caused by single I = 1/2 isobars of spin 3/2 and 5/2, respectively.

In Fig. 14 the predictions for isobar production are compared with our observed results near $\theta_{c.m.}$ = 90 deg. The comparison indicates that the model is at least partially successful. Although the absolute normalization is wrong, the energy dependence of the cross sections and the relative amounts of $N^*(1238)$, $N^*(1512)$, and $N^*(1688)$ production are approximately reproduced by the model. The absence of other known isobars from our spectra constitutes weak evidence against the statistical model. The $N^*(1410)$ and $N^*(1920)$ are in mass regions where they could be observed in this experiment; but the predicted cross sections are small. The $N^*(1410)$ is suppressed relative to the $N^*(1512)$ and $N^*(1688)$ by the spin factor, and the $N^*(1920)$ is suppressed by the isospin Clebsch-Gordan factor. In addition the expected large widths for both $N^*(1410)$ and $N^*(1920)$ would make them difficult for us to locate above background. Our data probably do not rule out $N^*(1920)$ production in accordance with the model; but we estimate that we would have detected the $N^*(1410)$ if its cross section were as large as half that predicted by the statistical model.

It should be pointed out that at our energies the kinematic factors in Eq. (7) are relatively insensitive to the final-state baryon masses. Thus any model that predicted variations in isobar production cross sections in accord with the relevant spin-isospin statistical factors would compare similarly with these data. For example, it is clear that whatever the details of the interaction at large momentum transfers, sufficient excitation to produce any of the lower baryon states should occur. Hence a model based on the notion of "nuclear democracy"[23] might result in similar predictions.

In order to describe the kinematic dependence of our measured cross sections we have generalized the phenomenological formula which Akerlof et al.[16] used to fit elastic pp scattering at $\theta_{c.m.} = \pi/2$ (although, as they note, persistence of their functional form at high energies would violate the lower analyticity bound of Cerulus and Martin[24] and Kinoshita[25]). A conceptual difficulty in using $p_\perp{}^2$ (or $p_\perp$) to describe inelastic two-body processes is that $p_\perp$ is different for the direct and the inverse processes. A suitable generalization of $p_\perp{}^2$ in terms of the Mandelstam variables is provided by the function

$$v \equiv -[tu/(t+u)],$$

where $$t = (\underset{\sim}{p}_1 - \underset{\sim}{p}_3)^2 = -2p^2\,(1 - \cos\theta)$$

and $$u = (\underset{\sim}{p} - \underset{\sim}{p}_4)^2 = -2p^2\,(1 + \cos\theta).$$

For elastic scattering, $v \equiv p_\perp^2$.

For inelastic processes v has the following desirable properties that $p_\perp^2$ manifests for elastic scattering: it is symmetric under interchange of the initial-state protons, it takes the same value for the inverse process, and it reduces to (-t) for small $|t|$.

We find that a function of the form

$$\frac{d\sigma}{dt} = B \exp(-v/v_0) \quad (19)$$

usually provides good fits to our differential cross sections at fixed energy, as is shown in Figs. 15 through 18. The exponential slopes vary systematically with energy and depend on the particular reaction under consideration in the manner shown in Fig. 19. An understanding of these variations must await a detailed theory applicable over a wide range of momentum transfers at intermediate energies. But a striking feature of Fig. 19 is the tendency of all the slopes toward the same value ($v_0 \approx 0.4\ GeV^2$) at the upper end of our energy range. This regularity is consistent with the spirit of the Wu-Yang hypothesis.

A possible source of deviations from the isospin weights predicted by Eq. (7) is the electromagnetic interaction. Observing that the ep elastic scattering cross section falls with -t at about half the slope of the pp elastic cross section, Wu and Yang suggest that the explanation is that the latter process involves two, instead of one, extended objects that can "break-up" in an energetic collision.[17] Study of isobar production cross sections at higher energies and larger momentum transfers might help to resolve these questions.

REFERENCES AND FOOTNOTES

*Work done under auspices of the U. S. Atomic Energy Commission.

†Present address: Brookhaven National Laboratory, Upton, L. I., N. Y.

1. G. Cocconi, A. N. Diddens, E. Lillethun, G. Manning, A. E. Taylor, T. G. Walker, and A. M. Wetherell, Phys. Rev. Letters 7, 450 (1961).

2. G. B. Chadwick, G. B. Collins, P. J. Duke, T. Fujii, N. C. Hien, M. A. R. Kemp, and F. Turkot, Phys. Rev. 128, 1823 (1962).

3. G. Cocconi, E. Lillethun, J. P. Scanlon, C. A. Stahlbrandt, C. C. Ting, J. Walters, and A. M. Wetherell, Phys. Letters 8, 134 (1964).

4. G. Bellettini, G. Cocconi, A. N. Diddens, E. Lillethun, J. P. Scanlon, A. M. Shapiro, and A. M. Wetherell, Phys. Letters 18, 167 (1965).

5. C. M. Ankenbrandt, A. R. Clyde, Bruce Cork, D. Keefe, L. T. Kerth, W. M. Layson, and W. A. Wenzel, Nuovo Cimento 35, 1052 (1965).

6. E. W. Anderson, E. J. Bleser, G. B. Collins, T. Fujii, J. Menes, F. Turkot, R. A. Carrigan, Jr., R. M. Edelstein, N. C. Hien, T. J. McMahon, and I. Nadelhaft, Phys. Rev. Letters 16, 855 (1966).

7. I. M. Blair, A. E. Taylor, W. S. Chapman, P. I. P. Kalmus, J. Litt, M. C. Miller, D. B. Scott, H. J. Sherman, A. Astbury, and T. G. Walker, Phys. Rev. Letters 17, 789 (1966).

8. L. D. Roper, Phys. Rev. Letters 12, 340 (1964).

9. This work was the subject of a thesis (by this title) submitted by C. M. Ankenbrandt to the University of California, Berkeley, in

partial fulfillment of the requirements for the Ph. D. degree; Lawrence Radiation Laboratory Report UCRL-17257, August 1967 (unpublished).

10. G. Fast and R. Hagedorn, Nuovo Cimento 27, 208 (1963); G. Fast, R. Hagedorn, and L. W. Jones, Nuovo Cimento 27, 856 (1963).
11. R. Hagedorn, Nuovo Cimento 35, 216 (1965).
12. Jay Orear, Phys. Rev. Letters 12, 112 (1964).
13. J. Orear, Phys. Letters 13, 190 (1964).
14. A. R. Clyde, Bruce Cork, D. Keefe, L. T. Kerth, W. M. Layson, and W. A. Wenzel (UCRL-11441, 1964), presented at XII Inter-National Conference on High Energy Physics, Dubna (1964); Allan R. Clyde, Ph. D. thesis, Lawrence Radiation Laboratory Report UCRL-16275, May 1966).
15. J. V. Allaby, G. Bellettini, G. Cocconi, A. N. Diddens, M. L. Good, G. Matthiae, E. J. Sacharidis, A. Silverman, and A. M. Wetherell, Phys. Letters 23, 389 (1966); J. V. Allaby, G. Cocconi, A. N. Diddens, A. Klovning, G. Matthiae, E. J. Sacharidis, and A. M. Wetherell, Phys. Letters 25B, 156 (1967).
16. C. W. Akerlof, R. H. Hieber, A. C. Krisch, K. W. Edwards, L. G. Ratner, and K. Ruddick, Phys. Rev. Letters 17, 1105 (1966).
17. Tai Tsun Wu and C. N. Yang, Phys. Rev. 137B, 708 (1965).
18. C. M. Ankenbrandt, A. R. Clark, Bruce Cork, T. Elioff, L. T. Kerth, and W. A. Wenzel, IEEE Trans. Nucl. Sci. NS-12 No. 4-6, 113, (1965) (Proceedings of the Purdue Instrumentation Conference, May 12-14, 1965).

19. W. W. Chupp, T. Elioff, and W. A. Wenzel, The Improved Bevatron and Its Performance at High Intensity, Lawrence Radiation Laboratory Report UCRL-16228, Aug. 1965), presented at Vth International Conference on High Energy Accelerators, Frascati, Italy, September 9-16, 1965.

20. D. Luckey, in Techniques of High Energy Physics, Part IX, edited by David M. Ritson (Interscience Publishers, Inc., New York, 1961), p. 403.

21. Thomas J. Devlin, OPTIK-An IBM 709 Computer Program for the Optics of High-Energy Particle Beams, Lawrence Radiation Laboratory Report UCRL-9727, September 1961.

22. J. D. Jackson, Nuovo Cimento 34, 1644 (1964).

23. See, for example, G. F. Chew, The Analytic S-Matrix: A Basis for Nuclear Democracy (W. A. Benjamin Inc., New York, 1966).

24. F. Cerulus and A. Martin, Phys. Letters 8, 80 (1964).

25. T. Kinoshita, Phys. Rev. Letters 12, 257 (1964).

Table I. Differential Cross Sections for pp → pp.

Nominal p_1 (GeV/c)	Corrected p_1 (GeV/c)	$-t$ (GeV^2)	$\frac{d\sigma}{dt}$ (mb/GeV^2)
3.0	2.98	0.27	$(1.6 \pm 0.4) \times 10^{+1}$
	2.98	0.39	$(8.9 \pm 0.7) \times 10^{+0}$
	2.98	0.58	$(3.2 \pm 0.2) \times 10^{+0}$
	2.98	0.68	$(2.1 \pm 0.2) \times 10^{+0}$
	2.98	0.79	$(1.48 \pm 0.09) \times 10^{+0}$
	2.98	0.94	$(1.06 \pm 0.05) \times 10^{+0}$
	2.98	0.94	$(1.05 \pm 0.05) \times 10^{+0}$
	2.98	1.34	$(6.3 \pm 0.3) \times 10^{-1}$
	2.98	1.75	$(4.7 \pm 0.3) \times 10^{-1}$
	2.98	1.98	$(4.3 \pm 0.2) \times 10^{-1}$
4.0	3.98	0.48	$(4.9 \pm 0.3) \times 10^{+0}$
	4.01	0.49	$(4.5 \pm 0.3) \times 10^{+0}$
	3.98	0.54	$(3.2 \pm 0.2) \times 10^{+0}$
	4.01	0.69	$(1.6 \pm 0.1) \times 10^{+0}$
	4.01	1.18	$(3.2 \pm 1.0) \times 10^{-1}$
	4.01	1.61	$(1.88 \pm 0.07) \times 10^{-1}$
	4.01	2.23	$(8.7 \pm 0.4) \times 10^{-2}$
	4.01	2.85	$(5.9 \pm 0.2) \times 10^{-2}$
5.0	4.98	0.73	$(9.5 \pm 0.6) \times 10^{-1}$
	5.01	0.75	$(1.05 \pm 0.08) \times 10^{+0}$
	5.01	0.75	$(1.07 \pm 0.08) \times 10^{+0}$
	4.98	0.83	$(6.3 \pm 0.4) \times 10^{-1}$
	5.01	0.84	$(7.1 \pm 0.5) \times 10^{-1}$
	4.98	1.03	$(3.2 \pm 0.3) \times 10^{-1}$
	5.01	1.04	$(3.3 \pm 0.2) \times 10^{-1}$
	4.98	1.52	$(1.0 \pm 0.1) \times 10^{-1}$
	4.98	1.76	$(6.4 \pm 0.5) \times 10^{-2}$
	5.05	1.80	$(6.0 \pm 0.3) \times 10^{-2}$
	4.98	2.80	$(2.1 \pm 0.1) \times 10^{-2}$
	4.98	3.08	$(1.98 \pm 0.07) \times 10^{-2}$
	4.98	3.23	$(1.68 \pm 0.04) \times 10^{-2}$
	4.98	3.59	$(1.5 \pm 0.1) \times 10^{-2}$
	4.98	3.64	$(1.64 \pm 0.04) \times 10^{-2}$
	4.98	3.64	$(1.47 \pm 0.07) \times 10^{-2}$
	4.98	3.80	$(1.9 \pm 0.2) \times 10^{-2}$

Table I. (continued)

Nominal p_1 (GeV/c)	Corrected p_1 (GeV/c)	$-t$ (GeV^2)	$\frac{d\sigma}{dt}$ (mb/GeV^2)
6.0	6.07	1.09	$(2.0 \pm 0.2) \times 10^{-1}$
	6.08	1.23	$(1.23 \pm 0.09) \times 10^{-1}$
	6.08	1.51	$(5.7 \pm 0.3) \times 10^{-2}$
	6.08	1.83	$(2.9 \pm 0.2) \times 10^{-2}$
	6.08	2.18	$(1.7 \pm 0.1) \times 10^{-2}$
	6.08	2.18	$(1.7 \pm 0.2) \times 10^{-2}$
	6.08	2.18	$(1.7 \pm 0.2) \times 10^{-2}$
	6.08	2.51	$(1.21 \pm 0.06) \times 10^{-2}$
	6.08	2.85	$(9.3 \pm 0.6) \times 10^{-3}$
	6.08	3.32	$(6.2 \pm 0.3) \times 10^{-3}$
	6.08	3.90	$(4.5 \pm 0.2) \times 10^{-3}$
	6.08	4.44	$(3.1 \pm 0.2) \times 10^{-3}$
	6.08	4.66	$(3.1 \pm 0.1) \times 10^{-3}$
	6.07	4.66	$(3.0 \pm 0.2) \times 10^{-3}$
	6.07	4.67	$(3.2 \pm 0.1) \times 10^{-3}$
7.0, 7.1	7.07	1.42	$(5.3 \pm 0.6) \times 10^{-2}$
	7.16	1.58	$(3.4 \pm 0.4) \times 10^{-2}$
	7.16	1.81	$(2.1 \pm 0.2) \times 10^{-2}$
	7.16	2.37	$(7.5 \pm 1.0) \times 10^{-3}$
	7.16	2.71	$(6.2 \pm 0.7) \times 10^{-3}$
	7.08	3.16	$(3.9 \pm 0.5) \times 10^{-3}$
	7.07	4.36	$(1.5 \pm 0.2) \times 10^{-3}$
	7.08	4.46	$(1.1 \pm 0.3) \times 10^{-3}$
	7.08	4.63	$(1.1 \pm 0.3) \times 10^{-3}$
	7.08	5.67	$(6.3 \pm 0.7) \times 10^{-4}$

Table II. Average masses and full widths of spectral peaks.

Symbol	Mass (MeV)	Γ (MeV)
$N^*(1238)$	1240±6	102±4
$N^*(1512)$	1508±2	92±3
$N^*(1688)$	1683±3	110±4

Table III. Differential cross sections for $pp \rightarrow pN^*(1238)$.

Nominal p_1 (GeV/c)	Corrected p_1 (GeV/c)	$-t$ (GeV^2)	$\frac{d\sigma}{dt}$ (mb/GeV^2)
3	2.98	0.26	$(1.5 \pm 0.2) \times 10^{+0}$
	2.98	0.29	$(9. \pm 1.) \times 10^{-1}$
	2.98	0.37	$(9. \pm 1.) \times 10^{-1}$
	2.98	0.64	$(3.9 \pm 0.4) \times 10^{-1}$
	2.98	0.74	$(3.9 \pm 0.4) \times 10^{-1}$
	2.98	0.88	$(3.1 \pm 0.3) \times 10^{-1}$
	2.98	1.26	$(1. \pm 0.2) \times 10^{-1}$
	2.98	1.63	$(1.5 \pm 0.2) \times 10^{-1}$
4	3.98	0.45	$(4.1 \pm 0.4) \times 10^{-1}$
	3.98	0.51	$(2.5 \pm 0.2) \times 10^{-1}$
	4.01	0.64	$(1.8 \pm 0.2) \times 10^{-1}$
	4.01	1.12	$(4.4 \pm 0.9) \times 10^{-2}$
	4.01	1.52	$(2.4 \pm 0.3) \times 10^{-2}$
	4.01	2.12	$(2.1 \pm 0.2) \times 10^{-2}$
	4.01	2.65	$(2.1 \pm 0.2) \times 10^{-2}$
5	5.01	0.70	$(7.6 \pm 0.8) \times 10^{-2}$
	5.01	0.80	$(4.3 \pm 0.6) \times 10^{-2}$
	5.01	0.99	$(2.4 \pm 0.3) \times 10^{-2}$
	5.02	1.46	$(1.2 \pm 0.3) \times 10^{-2}$
	5.05	1.72	$(5. \pm 1.) \times 10^{-3}$
	4.98	1.91	$(9. \pm 1.) \times 10^{-3}$
	4.98	2.67	$(3.5 \pm 0.5) \times 10^{-3}$
	4.98	3.08	$(2. \pm 1.) \times 10^{-3}$
6	6.08	1.03	$(1.1 \pm 0.3) \times 10^{-2}$
	6.08	1.16	$(1.1 \pm 0.3) \times 10^{-2}$
	6.08	1.44	$(9. \pm 3.) \times 10^{-3}$
	6.08	1.75	$(6.6 \pm 0.9) \times 10^{-3}$
	6.08	2.08	$(5. \pm 1.) \times 10^{-3}$
	6.08	2.40	$(3.0 \pm 0.6) \times 10^{-3}$
	6.08	2.73	$(2.1 \pm 0.4) \times 10^{-3}$
	6.08	3.18	$(9. \pm 1.) \times 10^{-4}$
	6.08	3.75	$(5. \pm 1.) \times 10^{-4}$
	6.08	4.25	$(4. \pm 2.) \times 10^{-4}$
7, 7.1	7.07	1.33	$(8. \pm 3.) \times 10^{-3}$
	7.16	1.50	$(5. \pm 1.) \times 10^{-3}$
	7.16	1.72	$(4.2 \pm 0.8) \times 10^{-3}$
	7.16	2.27	$(2.6 \pm 0.9) \times 10^{-3}$
	7.16	2.60	$(1.1 \pm 0.5) \times 10^{-3}$
	7.08	3.05	$(1. \pm 0.6) \times 10^{-3}$
	7.07	4.22	$(2.5 \pm 0.9) \times 10^{-4}$

Table IV. Differential cross sections for $pp \to pN^*(1512)$.

Nominal p_1 (GeV/c)	Corrected p_1 (GeV/c)	$-t$ (GeV^2)	$\frac{d\sigma}{dt}$ (mb/GeV^2)
4	3.98	0.44	$(2.5 \pm 0.4) \times 10^{-1}$
	3.98	0.50	$(2. \pm 0.2) \times 10^{-1}$
	4.01	0.62	$(1.5 \pm 0.2) \times 10^{-1}$
	4.01	1.06	$(1.5 \pm 0.2) \times 10^{-1}$
	4.01	1.43	$(1.20 \pm 0.09) \times 10^{-1}$
	4.01	1.99	$(9.2 \pm 0.6) \times 10^{-2}$
	4.01	2.05	$(1.22 \pm 0.09) \times 10^{-1}$
5	5.01	0.67	$(1. \pm 1.) \times 10^{-1}$
	5.01	0.76	$(1.05 \pm 0.09) \times 10^{-1}$
	5.01	0.94	$(8.8 \pm 0.6) \times 10^{-2}$
	5.02	1.38	$(7. \pm 1.) \times 10^{-2}$
	5.05	1.61	$(5.2 \pm 0.6) \times 10^{-2}$
	4.98	1.79	$(5.7 \pm 0.5) \times 10^{-2}$
	4.98	2.49	$(3.7 \pm 0.3) \times 10^{-2}$
	4.98	2.83	$(3. \pm 1.) \times 10^{-2}$
	4.98	2.86	$(3.1 \pm 0.5) \times 10^{-2}$
	4.98	3.14	$(2.5 \pm 0.5) \times 10^{-2}$
6	6.08	0.98	$(6.6 \pm 0.6) \times 10^{-2}$
	6.08	1.10	$(6.3 \pm 0.6) \times 10^{-2}$
	6.08	1.36	$(5.9 \pm 0.8) \times 10^{-2}$
	6.08	1.65	$(3.2 \pm 0.3) \times 10^{-2}$
	6.08	1.97	$(2.8 \pm 0.4) \times 10^{-2}$
	6.08	2.27	$(1.9 \pm 0.2) \times 10^{-2}$
	6.08	2.58	$(1.4 \pm 0.1) \times 10^{-2}$
	6.08	3.00	$(1.07 \pm 0.07) \times 10^{-2}$
	6.08	3.52	$(8.2 \pm 0.6) \times 10^{-3}$
	6.07	3.89	$(7. \pm 1.) \times 10^{-3}$
	6.08	4.02	$(6.4 \pm 0.8) \times 10^{-3}$
7, 7.1	7.07	1.27	$(3.5 \pm 0.5) \times 10^{-2}$
	7.16	1.43	$(2.9 \pm 0.4) \times 10^{-2}$
	7.16	1.64	$(2.0 \pm 0.3) \times 10^{-2}$
	7.16	2.16	$(7. \pm 1.) \times 10^{-3}$
	7.16	2.47	$(7. \pm 1.) \times 10^{-3}$
	7.08	2.89	$(3.2 \pm 0.8) \times 10^{-3}$
	7.07	4.01	$(2.3 \pm 0.4) \times 10^{-3}$
	7.08	5.01	$(1.3 \pm 0.3) \times 10^{-3}$

Table V. Differential cross sections for $pp \rightarrow pN^*(1688)$.

Nominal p_1 (GeV/c)	Corrected p_1 (GeV/c)	$-t$ (GeV^2)	$\frac{d\sigma}{dt}$ (mb/GeV^2)
4	3.98	0.47	$(6.6 \pm 0.9) \times 10^{-1}$
	3.98	0.52	$(3.4 \pm 0.3) \times 10^{-1}$
	4.01	0.64	$(4.5 \pm 0.4) \times 10^{-1}$
	4.01	1.05	$(2.3 \pm 0.3) \times 10^{-1}$
	4.01	1.40	$(1.6 \pm 0.1) \times 10^{-1}$
	4.01	1.93	$(1.29 \pm 0.09) \times 10^{-1}$
5	5.01	0.67	$(2.3 \pm 0.2) \times 10^{-1}$
	5.01	0.75	$(1.8 \pm 0.2) \times 10^{-1}$
	5.01	0.92	$(1.2 \pm 0.1) \times 10^{-1}$
	5.02	1.33	$(9. \pm 1.) \times 10^{-2}$
	5.05	1.55	$(7.8 \pm 0.8) \times 10^{-2}$
	4.98	1.73	$(7.4 \pm 0.7) \times 10^{-2}$
	4.98	2.39	$(5.1 \pm 0.4) \times 10^{-2}$
	4.98	2.74	$(4.3 \pm 0.8) \times 10^{-2}$
6	6.08	0.95	$(9.3 \pm 0.8) \times 10^{-2}$
	6.08	1.07	$(8.9 \pm 0.9) \times 10^{-2}$
	6.08	1.32	$(5.8 \pm 0.8) \times 10^{-2}$
	6.08	1.59	$(4.3 \pm 0.4) \times 10^{-2}$
	6.08	1.90	$(2.9 \pm 0.4) \times 10^{-2}$
	6.08	2.18	$(2.0 \pm 0.2) \times 10^{-2}$
	6.08	2.47	$(1.3 \pm 0.1) \times 10^{-2}$
	6.08	2.88	$(1.08 \pm 0.08) \times 10^{-2}$
	6.08	3.38	$(7.7 \pm 0.8) \times 10^{-3}$
	6.08	3.85	$(8. \pm 1.) \times 10^{-3}$
7, 7.1	7.07	1.23	$(5.0 \pm 0.7) \times 10^{-2}$
	7.16	1.38	$(4.5 \pm 0.6) \times 10^{-2}$
	7.16	1.59	$(2.8 \pm 0.4) \times 10^{-2}$
	7.16	2.08	$(1.0 \pm 0.2) \times 10^{-2}$
	7.16	2.38	$(7. \pm 1.) \times 10^{-3}$
	7.08	2.79	$(4. \pm 1.) \times 10^{-3}$
	7.07	3.86	$(2.4 \pm 0.4) \times 10^{-3}$

FIGURE CAPTIONS

Fig. 1. Schematic diagram of the experimental apparatus. In the drawing B_i represent bending magnets, Q_i are quadrupole magnets, S_i are scintillation counters, and C_i are Cerenkov counters. C_1 and C_2 are lowered out of the beam when not in use.

Fig. 2. Trajectories of charged particles through the beam optical system. In the plan view parallel rays are traced; in the elevation view rays emanating from a point on the target are shown. These rays illustrate the focusing conditions for central-momentum particles.

Fig. 3. The geometry of the scintillators. S_2 and S_3 are in coincidence with H_i and $\overline{A}$ is in anticoincidence.

Fig. 4. Results of a typical elastic peak run. This spectrum was obtained at 5 GeV/c and θ_3 = 10.3 deg.

Fig. 5. Differential cross sections for elastic proton-proton scattering resulting from this experiment. Here and throughout this paper, error bars that are not shown are smaller than the size of the points.

Fig. 6. Comparison of our elastic data with those of Clyde et al. (Ref. 14) at (a) 3 GeV/c, (b) 5 GeV/c, (c) 7 GeV/c.

Fig. 7. Missing mass spectra at (a) p_1 = 6 GeV/c, θ_3 = 10.26 deg, (b) 7 GeV/c, 10.07 deg, and (c) 7 GeV/c, 13.49 deg, illustrating the lack of structure above the peak near 1688 MeV.

Fig. 8. Missing mass spectra at 3 GeV/c and lab angles of (a) 10.19, (b) 10.91, (c) 12.30, (d) 16.90, (e) 18.36, (f) 20.36, (g) 25.42, and (h) 30.48 deg. All the spectra are plotted to the same scale, with successive spectra displaced vertically by equal increments of 2 mb/GeV^4.

The solid curves are background estimates calculated with the fitting procedure of Section IV C. The small narrow peak between 1500 and 1600 MeV, especially noticeable in (d) through (f), is attributable to pions from the reaction pp → π^+d.

Fig. 9. Missing mass spectra at 4 GeV/c and lab angles of (a) 10.19, (b) 10.90, (c) 12.31, (d) 16.89, (e) 20.40, (f) 25.45, and (g) 30.55 deg. All the spectra are plotted to the same scale, with successive spectra displaced vertically by equal increments of 0.5 mb/GeV^4. The solid curves are background estimates calculated with the fitting procedure of Section IV C.

Fig. 10. Missing mass spectra at 5 GeV/c and lab angles of (a) 10.24, (b) 10.96, (c) 12.34, (d) 15.42, (e) 16.84, (f) 18.32, (g) 22.83, (h) 25.26, (i) 27.65, and (j) 29.99. All the spectra are plotted to the same scale, with successive spectra displaced vertically by equal increments of 0.2 mb/GeV^4. The solid curves are background estimates calculated with the fitting procedure of Section IV C.

Fig. 11. Missing mass spectra at 6 GeV/c and angles of (a) 10.26, (b) 10.95, (c) 12.34, (d) 13.86, (e) 15.42, (f) 16.84, (g) 18.32, (h) 20.31, (i) 22.81, (j) 25.27, and (k) 27.76 deg. All the spectra are plotted to the same scale, with successive spectra displaced vertically by equal increments of 0.05 mb/GeV^4. The solid curves are background estimates calculated with the fitting procedure of Section IV C.

Fig. 12. Missing mass spectra at 7 GeV/c and lab angles of (a) 10.07, (b) 10.59, (c) 11.48, (d) 13.49, (e) 14.65, (f) 16.44, (g) 20.58, and (h) 25.47 deg. All the spectra are plotted to the same scale, with

successive spectra displaced vertically by equal increments of 0.05 mb/GeV^4. The solid curves are background estimates calculated with the fitting procedure of Section IV C.

Fig. 13. Differential cross sections $d\sigma/dt$ for production of (a) N^* (1238), (b) N^*(1512), and (c) N^*(1688) vs (-t), the squared four-momentum transfer, at 3, 4, 5, 6, and 7 GeV/c. The straight lines are fits to the data of Blair et al. (Ref. 7) at the indicated momenta.

Fig. 14. Comparison of our N^* production cross sections near $\theta_{c.m.}$ = 90 deg with the predictions according to the statistical model of Hagedorn (Ref. 11).

Fig. 15. Differential cross sections for pp elastic scattering vs v at (a) 3, (b) 4, (c) 5, (d) 6, and (e) 7 GeV/c. The straight lines are least-squares fits to the data away from the diffraction peak. The reason for this choice of independent variable is explained in the text. Note that the vertical scale is displaced by a decade between successive curves.

Fig. 16. Differential cross sections for the process $pp \rightarrow pN^*(1238)$ vs v at (a) 3, (b) 4, (c) 5, (d) 6, and (e) 7 GeV/c. The straight lines are least-squares fits to all the data. Note that the vertical scale is displaced by a decade between successive curves.

Fig. 17. Differential cross sections for the process $pp \rightarrow pN^*(1512)$ vs v at (a) 4, (b) 5, (c) 6, and (d) 7 GeV/c. The straight lines are least-squares fits to all the data. Note that the vertical scale is displaced by a decade between successive curves.

Fig. 18. Differential cross sections for the process $pp \rightarrow pN^*(1688)$ vs v at (a) 4, (b) 5, (c) 6, and (d) 7 GeV/c. The straight lines are

least-squares fits to all the data. Note that the vertical scale is displaced by a decade between successive curves.

Fig. 19. The slope parameters of the fits shown in Figs. 15 through 18 as functions of the incident momentum.

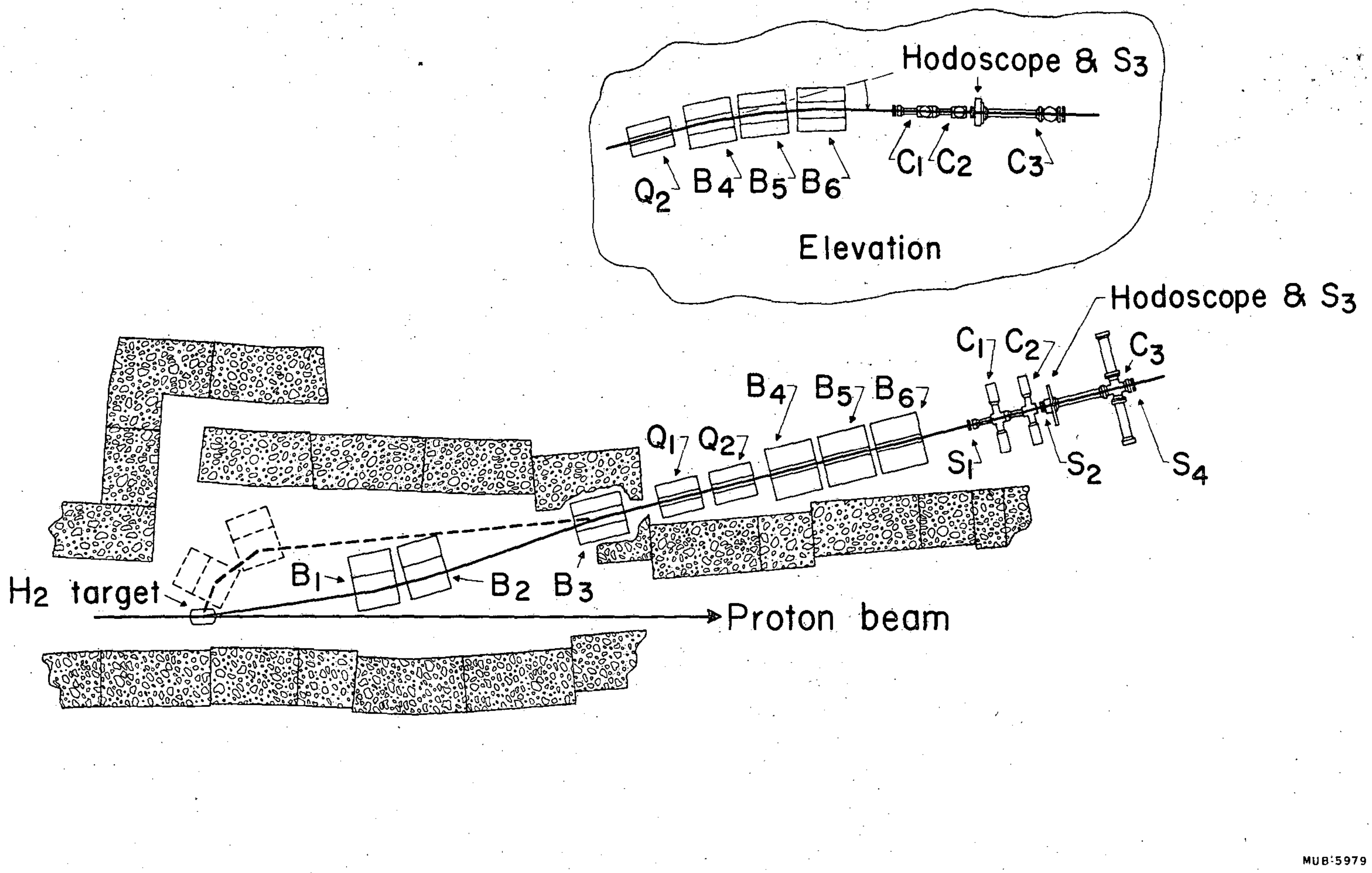
Hodoscope & S_3
Q_2
B_4
B_5
B_6
C_1
C_2
C_3
Elevation
Hodoscope & S_3
C_1
C_2
C_3
B_4
B_5
B_6
Q_1
Q_2
S_1
S_2
S_4
H_2 target
B_1
B_2
B_3
Proton beam
MUB-5979

Fig. 1

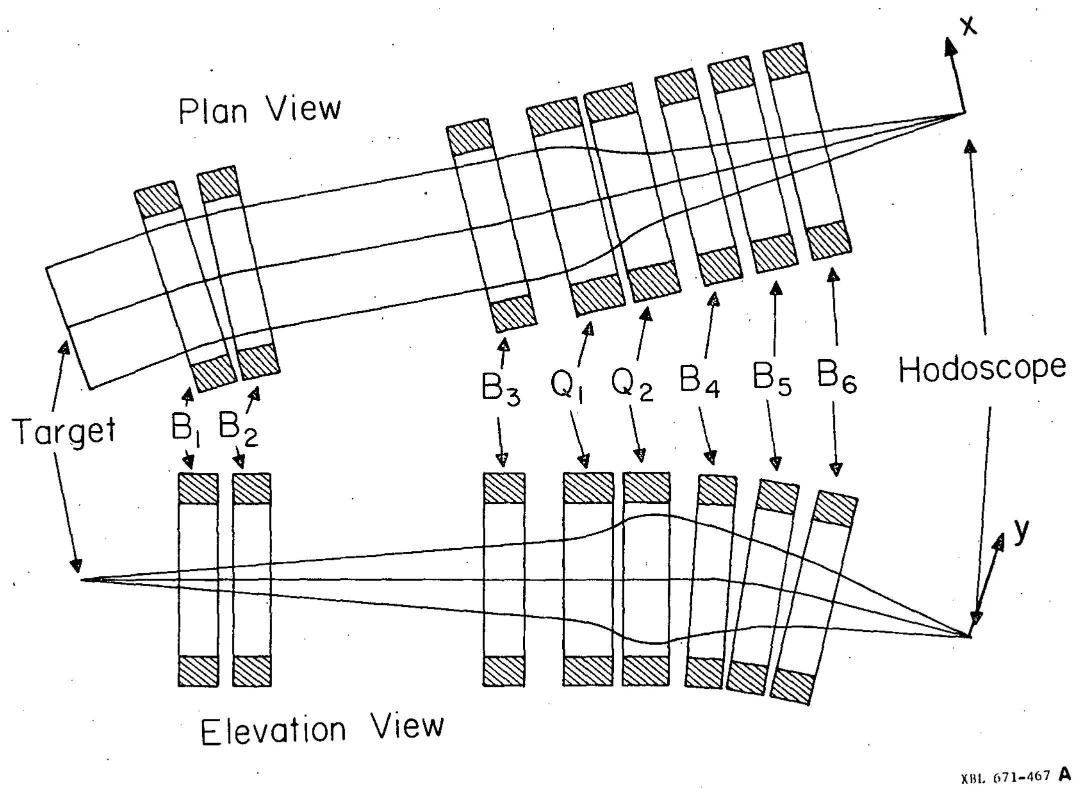

x
Plan View
Target
B_1
B_2
B_3
Q_1
Q_2
B_4
B_5
B_6
Hodoscope
y
Elevation View
XBL 671-467 A

Fig. 2

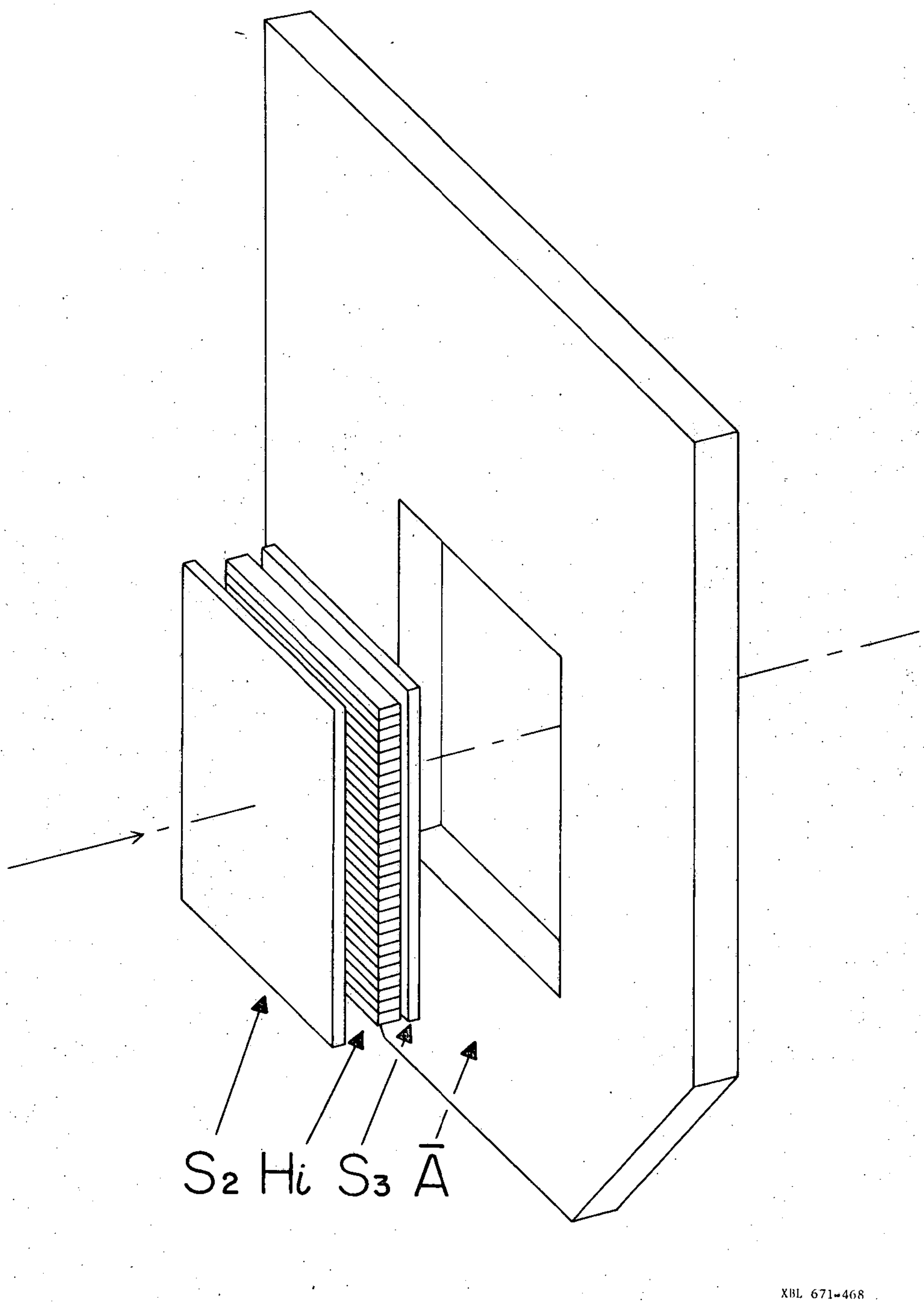

Fig. 3

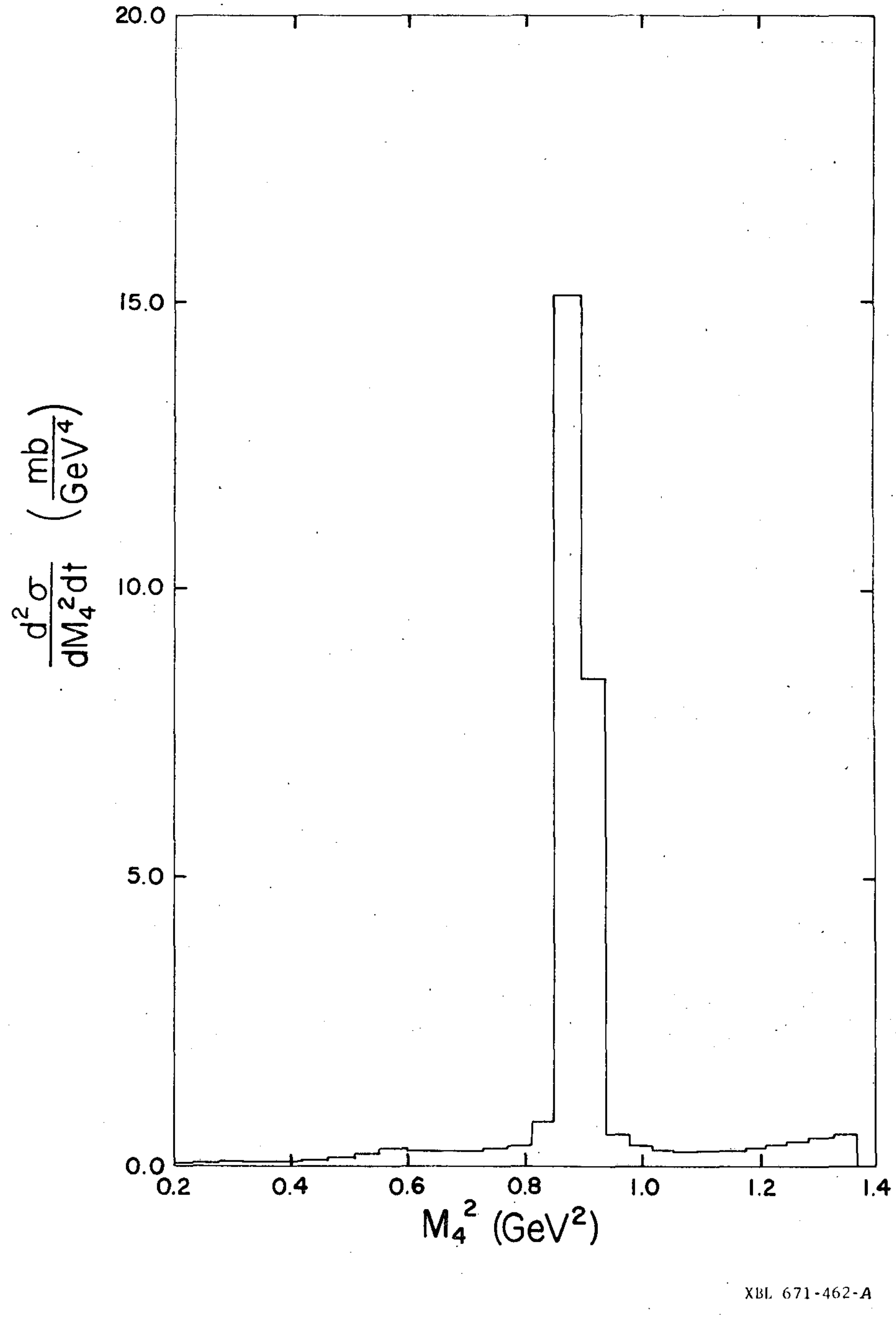

XBL 671-462-A

Fig. 4

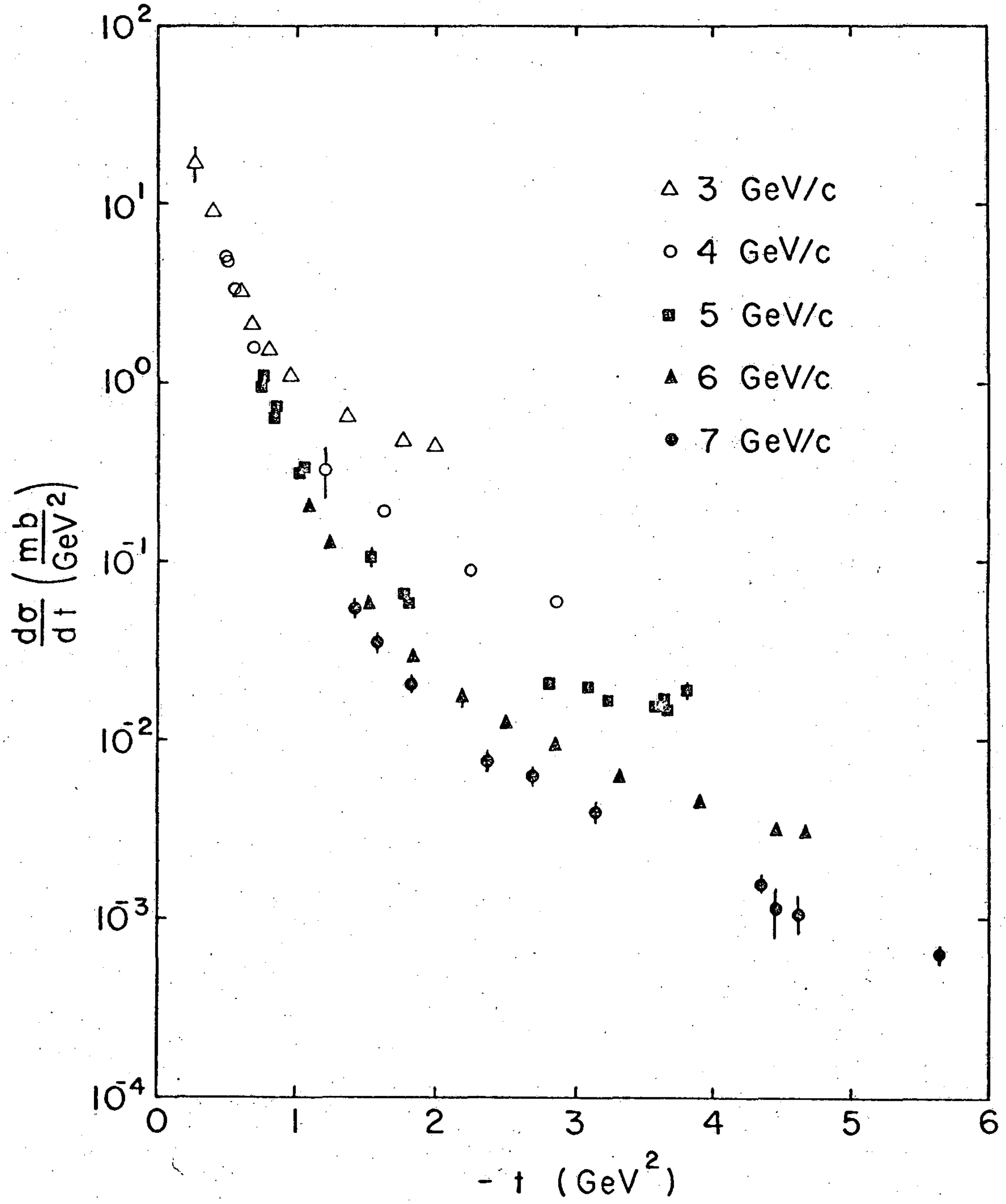

XBL 671-475-A

Fig. 5

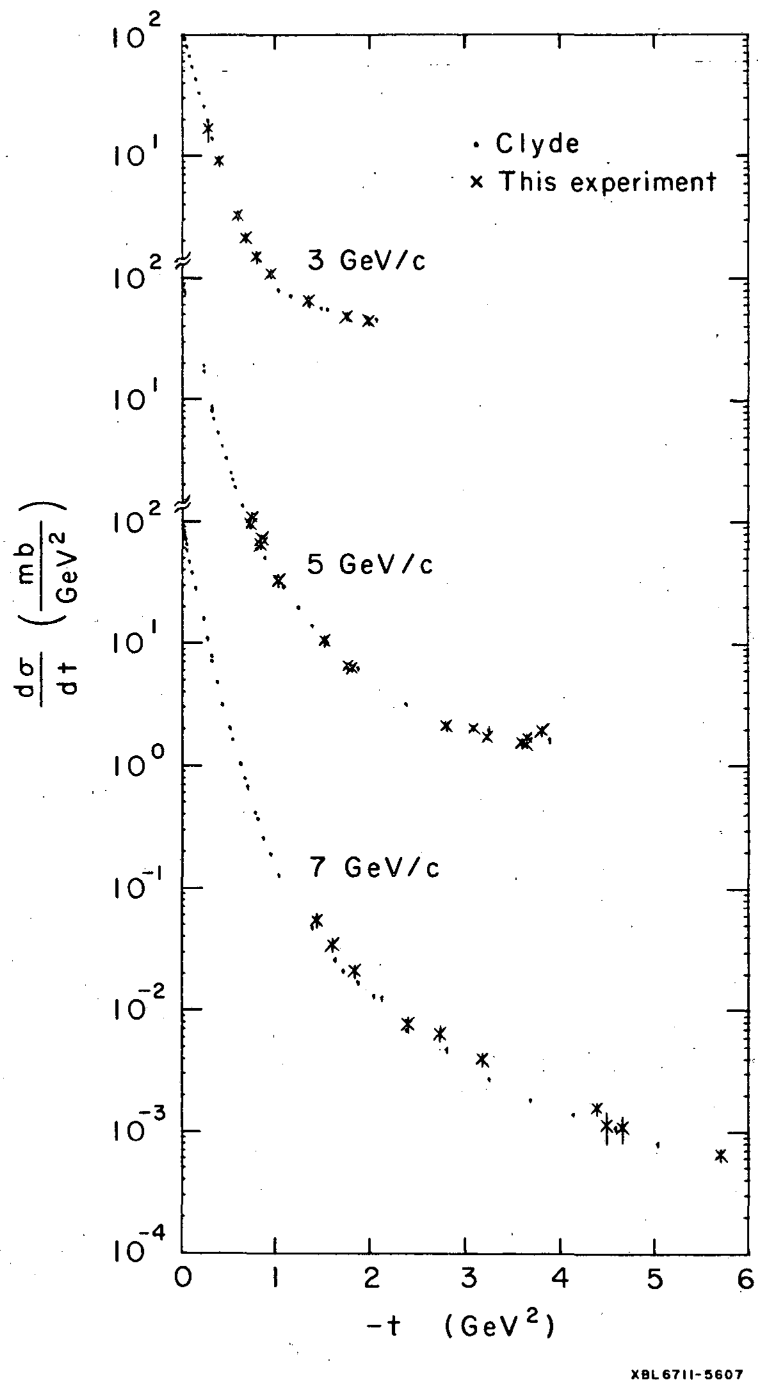

10^2
10^1
10^2
10^1
10^2
10^1
10^0
10^{-1}
10^{-2}
10^{-3}
10^{-4}
• Clyde
× This experiment
3 GeV/c
5 GeV/c
7 GeV/c
$\frac{d\sigma}{dt}\left(\frac{mb}{GeV^2}\right)$
0 1 2 3 4 5 6
$-t$ (GeV^2)
XBL 6711-5607

Fig. 6

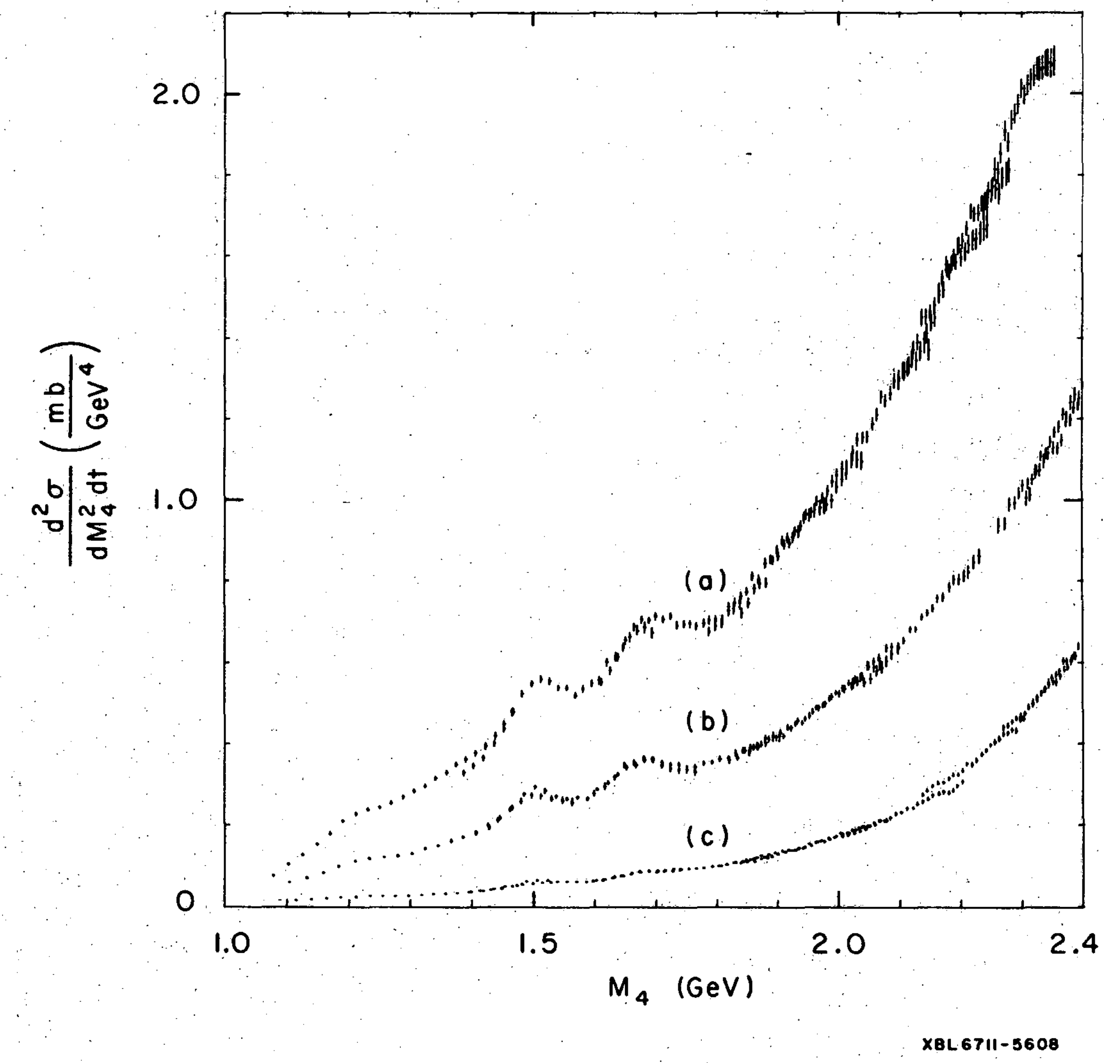
2.0
1.0
0
1.0
1.5
2.0
2.4
(a)
(b)
(c)
M$_4$ (GeV)
$\frac{d^2\sigma}{dM_4^2 dt}$ $\left(\frac{mb}{GeV^4}\right)$
XBL 6711-5608

Fig. 7

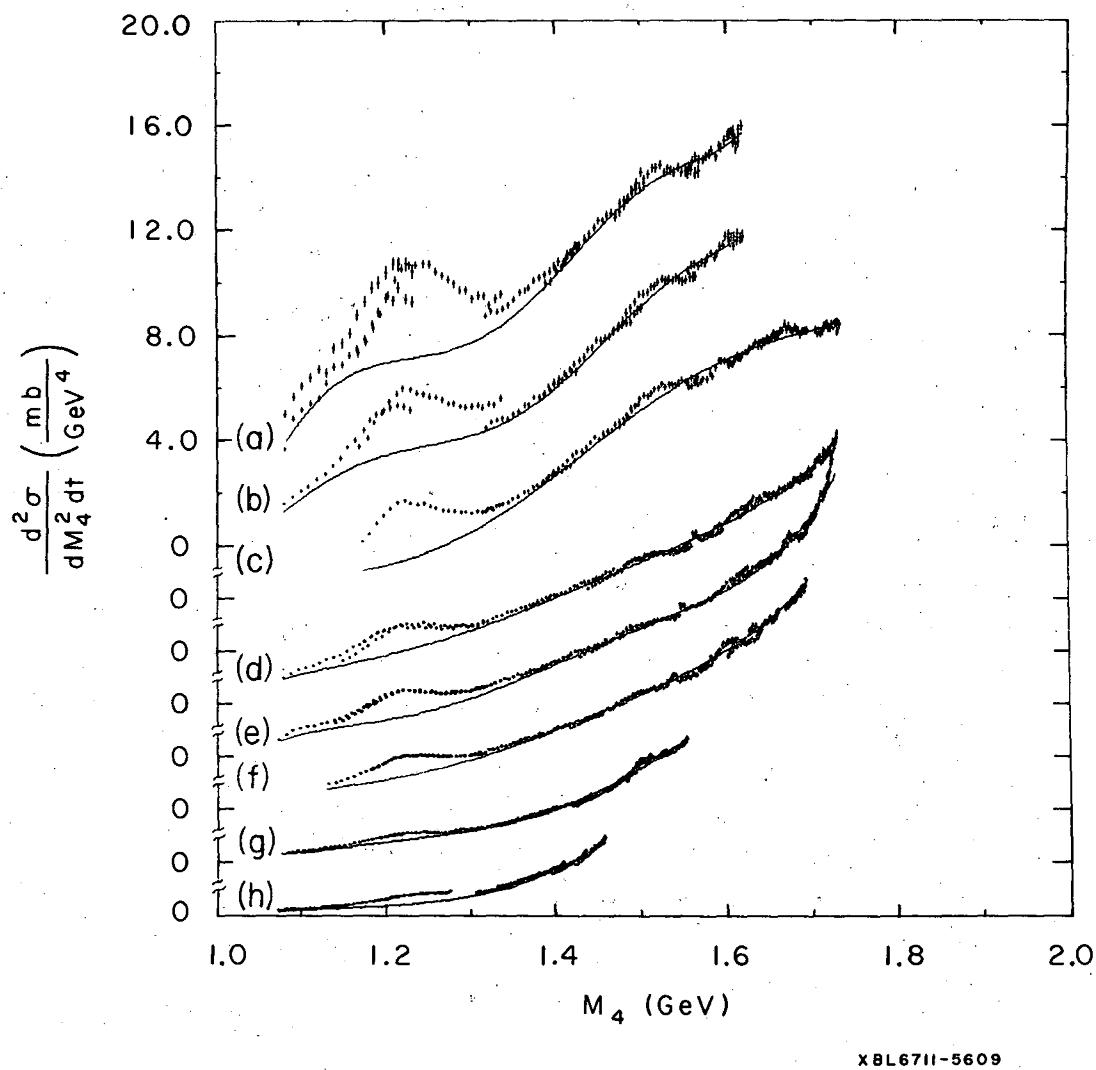
20.0
16.0
12.0
8.0
4.0
0
$\frac{d^2\sigma}{dM_4^2 dt}$ $\left(\frac{mb}{GeV^4}\right)$
(a)
(b)
(c)
(d)
(e)
(f)
(g)
(h)
1.0
1.2
1.4
1.6
1.8
2.0
M_4 (GeV)
XBL6711-5609

Fig. 8

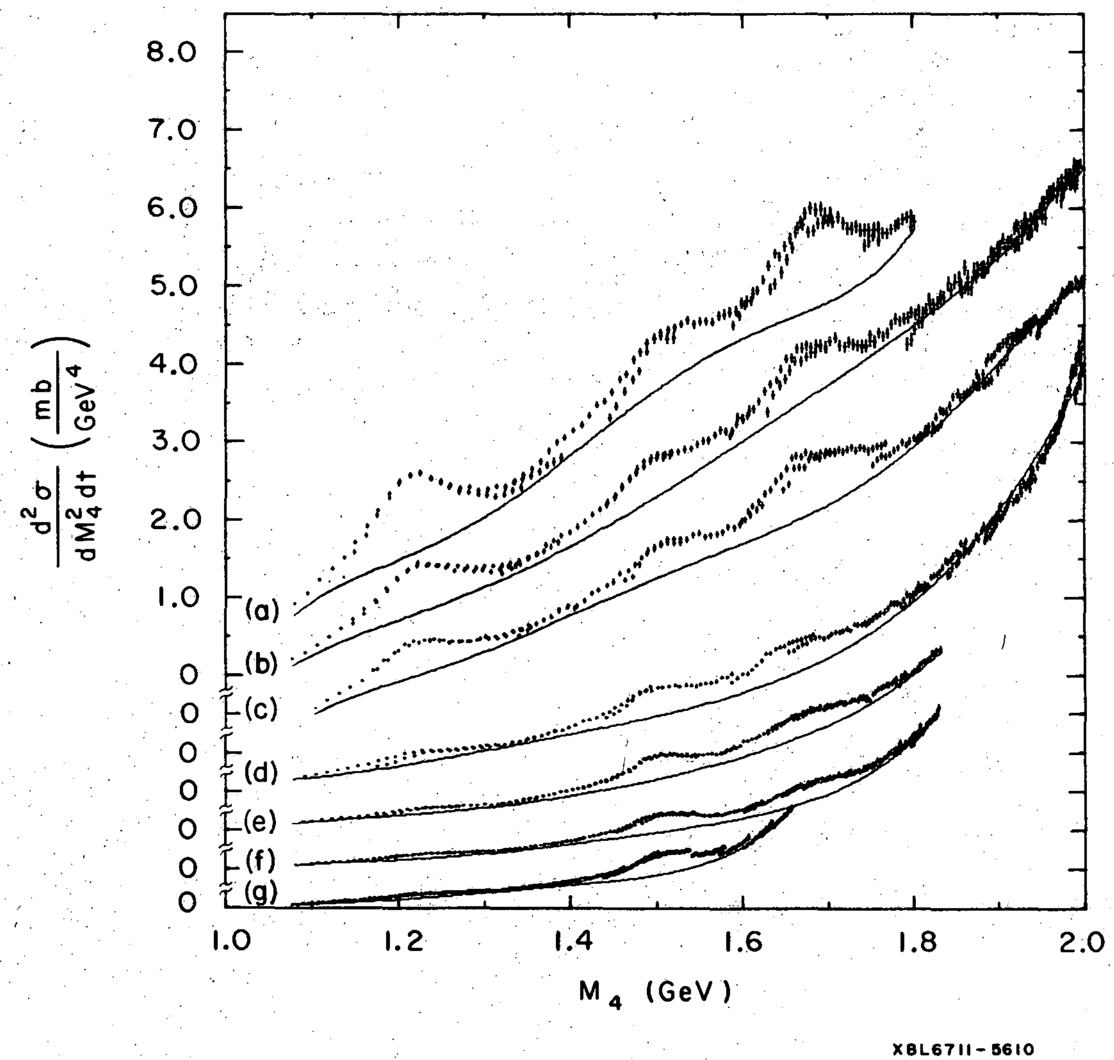
8.0
7.0
6.0
5.0
4.0
3.0
2.0
1.0
0
0
0
0
0
0
0
(a)
(b)
(c)
(d)
(e)
(f)
(g)
1.0
1.2
1.4
1.6
1.8
2.0
M 4 (GeV)
XBL6711-5610

Fig. 9

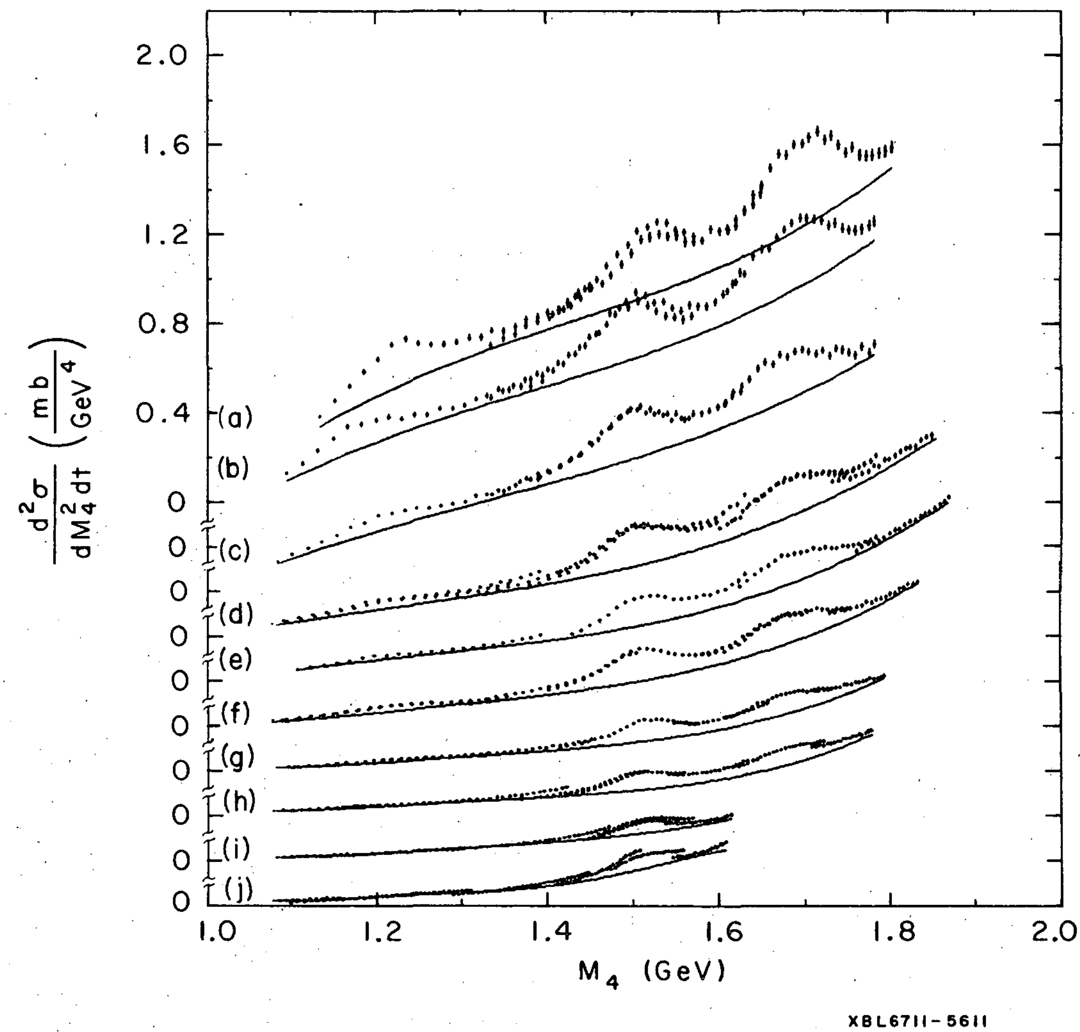
2.0
1.6
1.2
0.8
0.4
0
$\frac{d^2\sigma}{dM_4^2 dt}$ $\left(\frac{mb}{GeV^4}\right)$
(a)
(b)
(c)
(d)
(e)
(f)
(g)
(h)
(i)
(j)
1.0
1.2
1.4
1.6
1.8
2.0
M_4 (GeV)
XBL6711-5611

Fig. 10

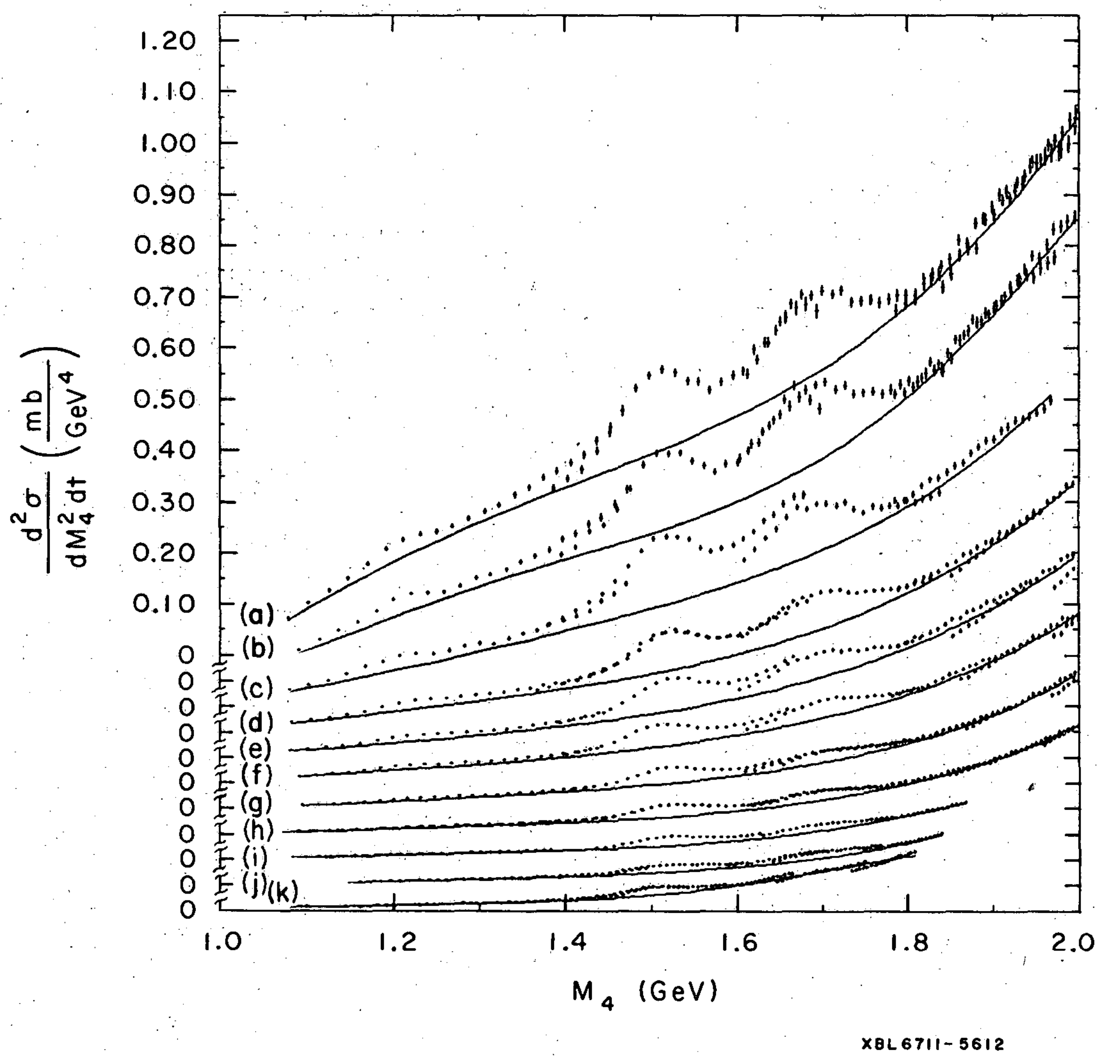
1.20
1.10
1.00
0.90
0.80
0.70
0.60
0.50
0.40
0.30
0.20
0.10
0
$\frac{d^2\sigma}{dM_4^2 dt}$ $\left(\frac{mb}{GeV^4}\right)$
(a)
(b)
(c)
(d)
(e)
(f)
(g)
(h)
(i)
(j)
(k)
1.0
1.2
1.4
1.6
1.8
2.0
M_4 (GeV)
XBL6711-5612

Fig. 11

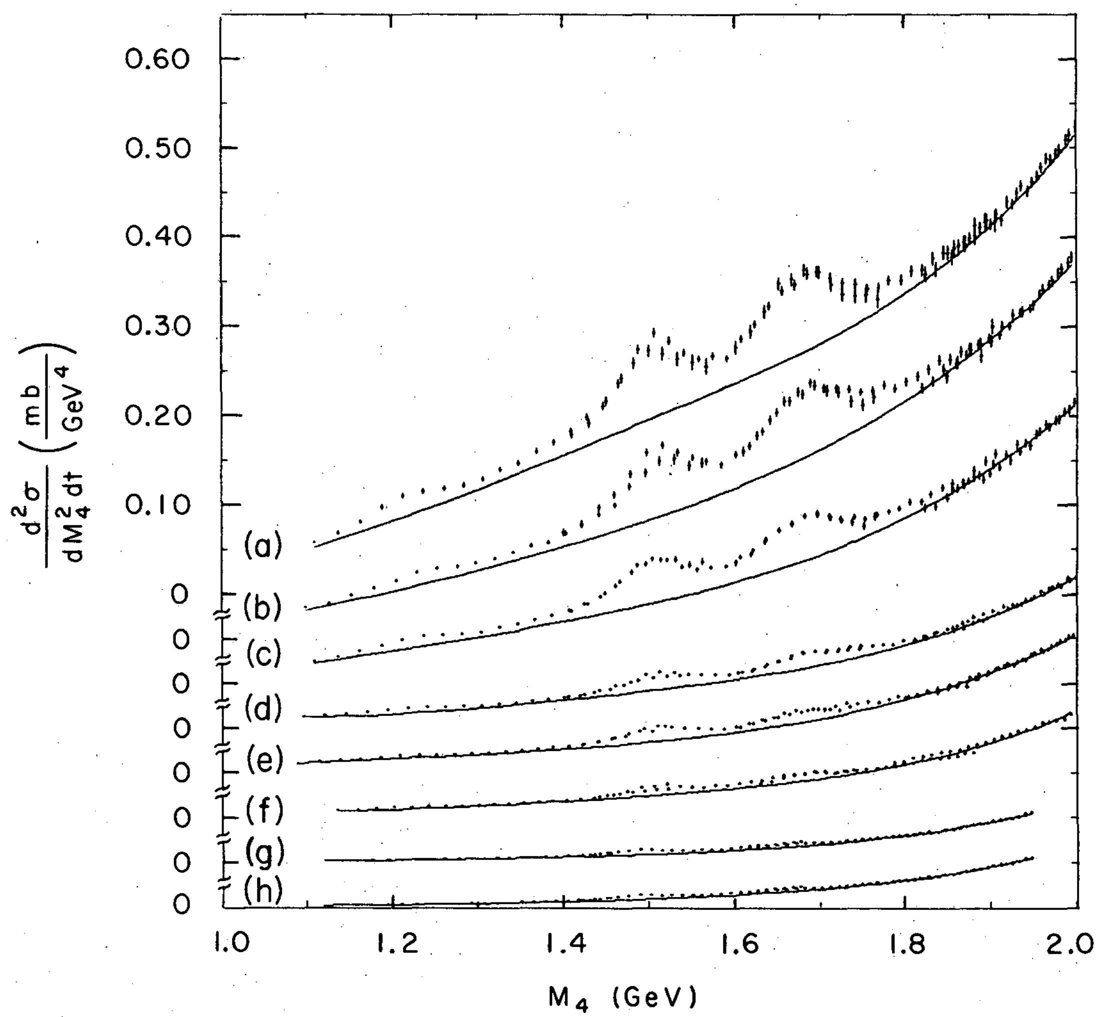

XBL6711-5613

Fig. 12

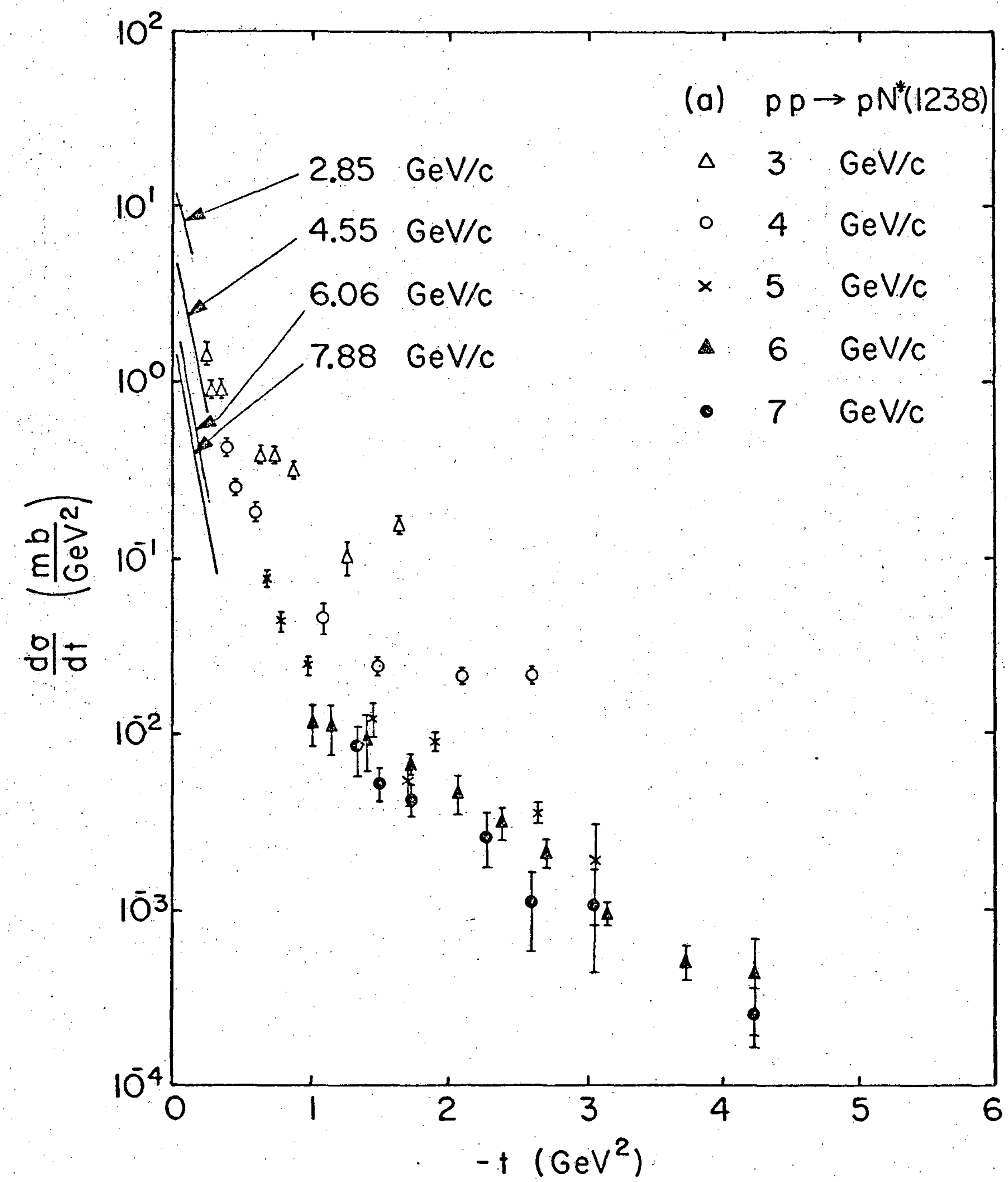

XBL 671-474-A

Fig. 13(a)

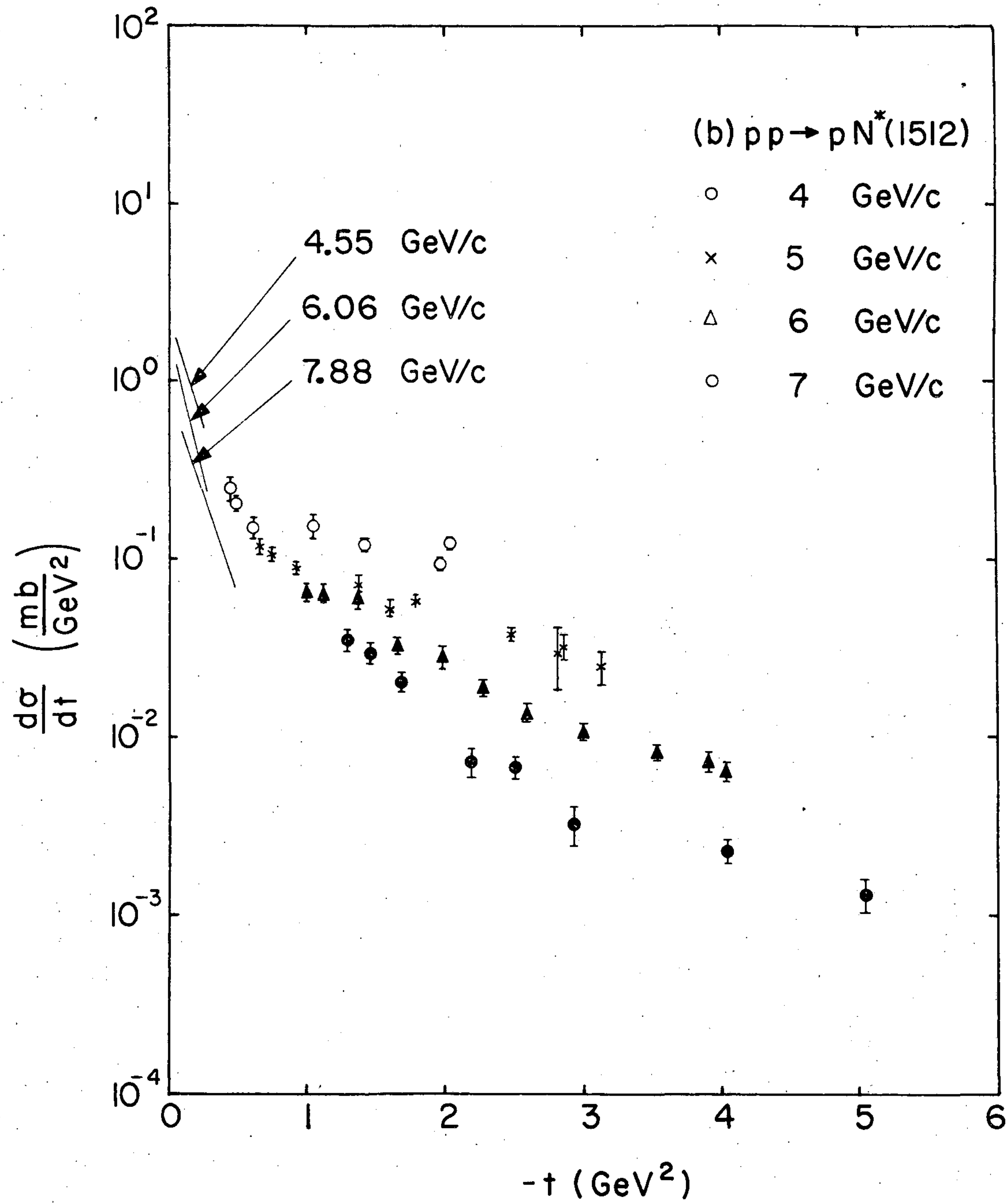
(b) pp → pN*(1512)
4 GeV/c
5 GeV/c
6 GeV/c
7 GeV/c
4.55 GeV/c
6.06 GeV/c
7.88 GeV/c
dσ/dt (mb/GeV²)
-t (GeV²)
XBL 671-516-A

Fig. 13(b)

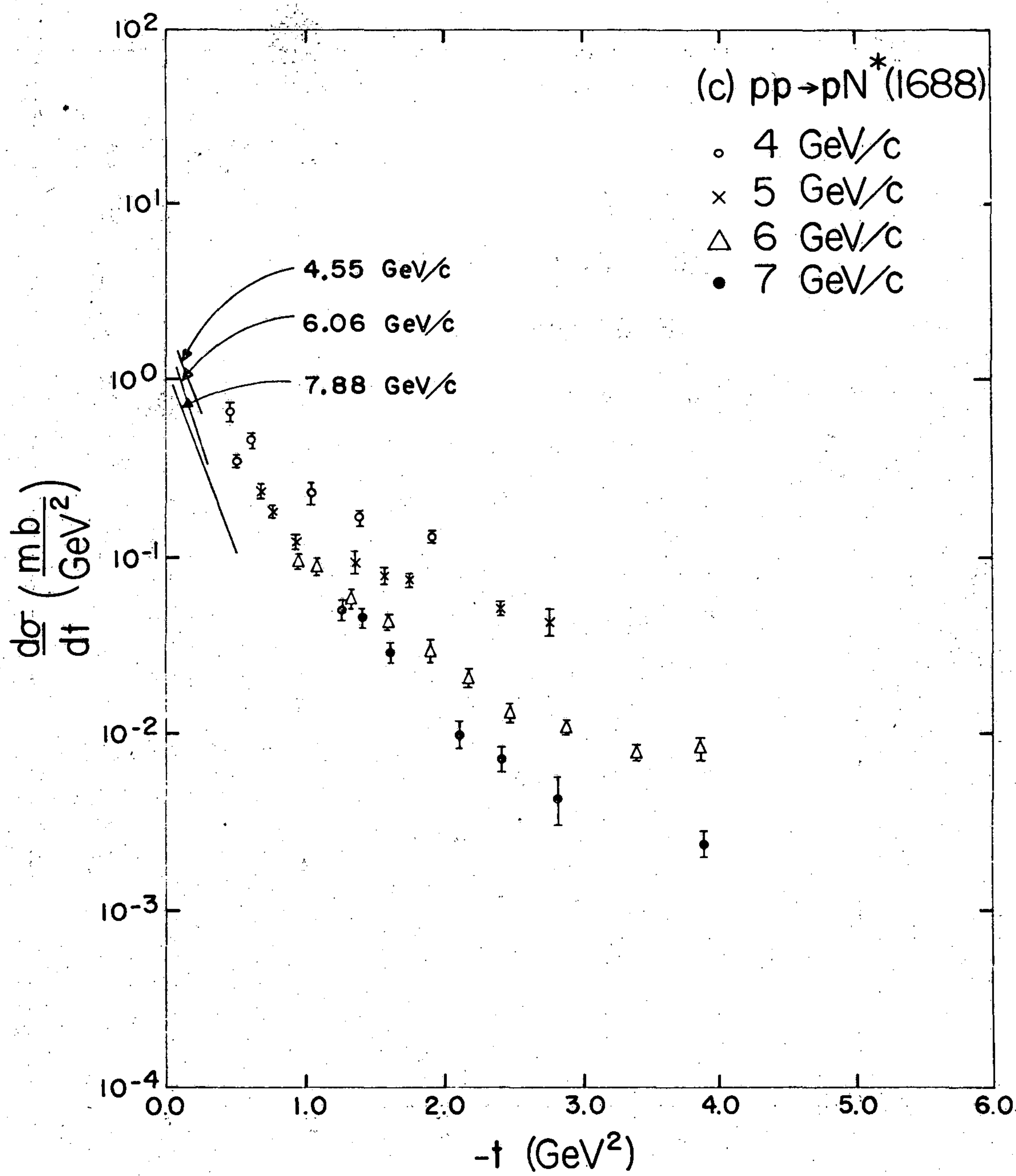

XBL 671-515-A

Fig. 13(c)

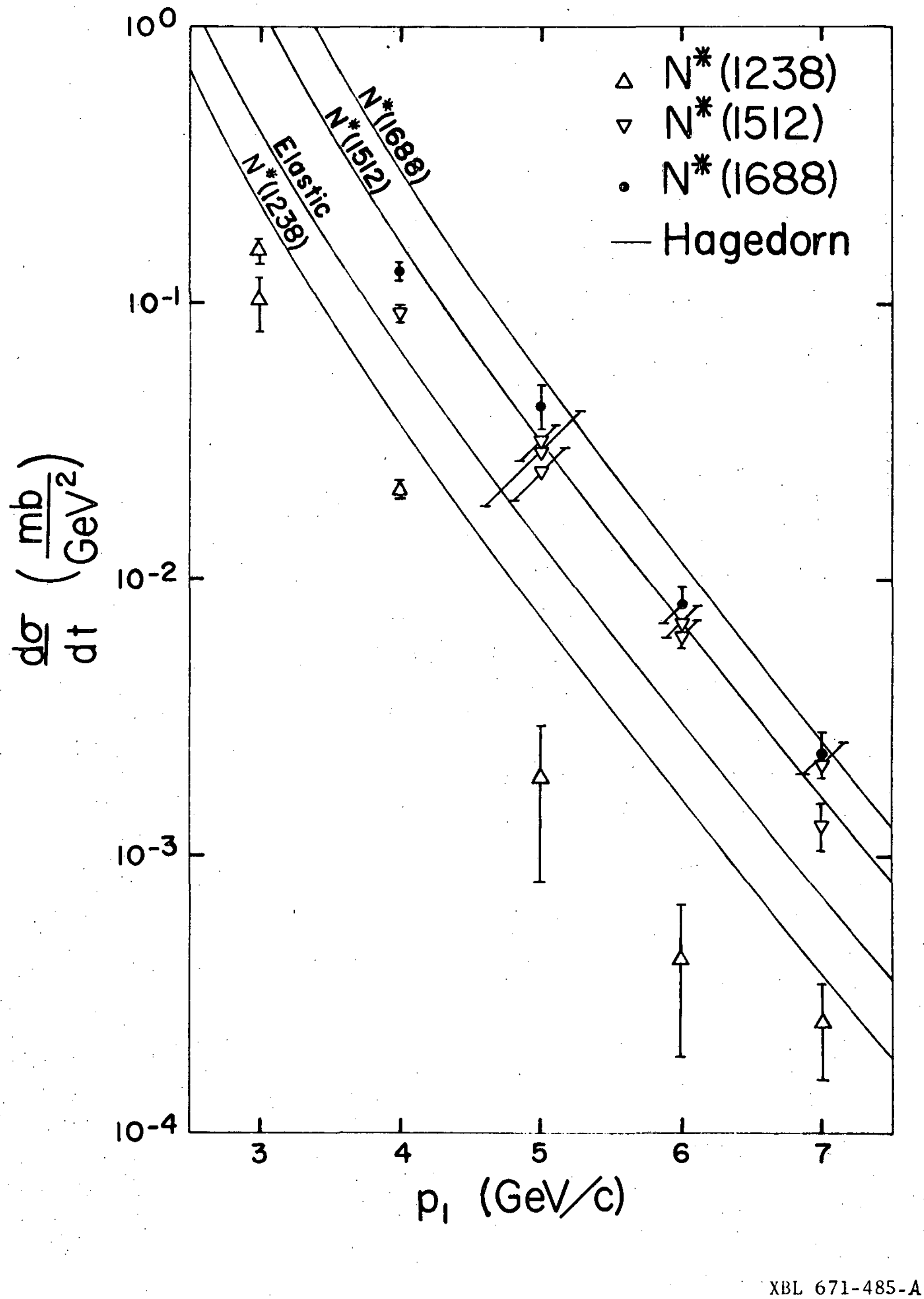
10^0
10^-1
10^-2
10^-3
10^-4
dσ/dt (mb/GeV^2)
3
4
5
6
7
p_l (GeV/c)
N*(1238)
N*(1512)
N*(1688)
Hagedorn
Elastic
N*(1238)
N*(1512)
N*(1688)
XBL 671-485-A

Fig. 14

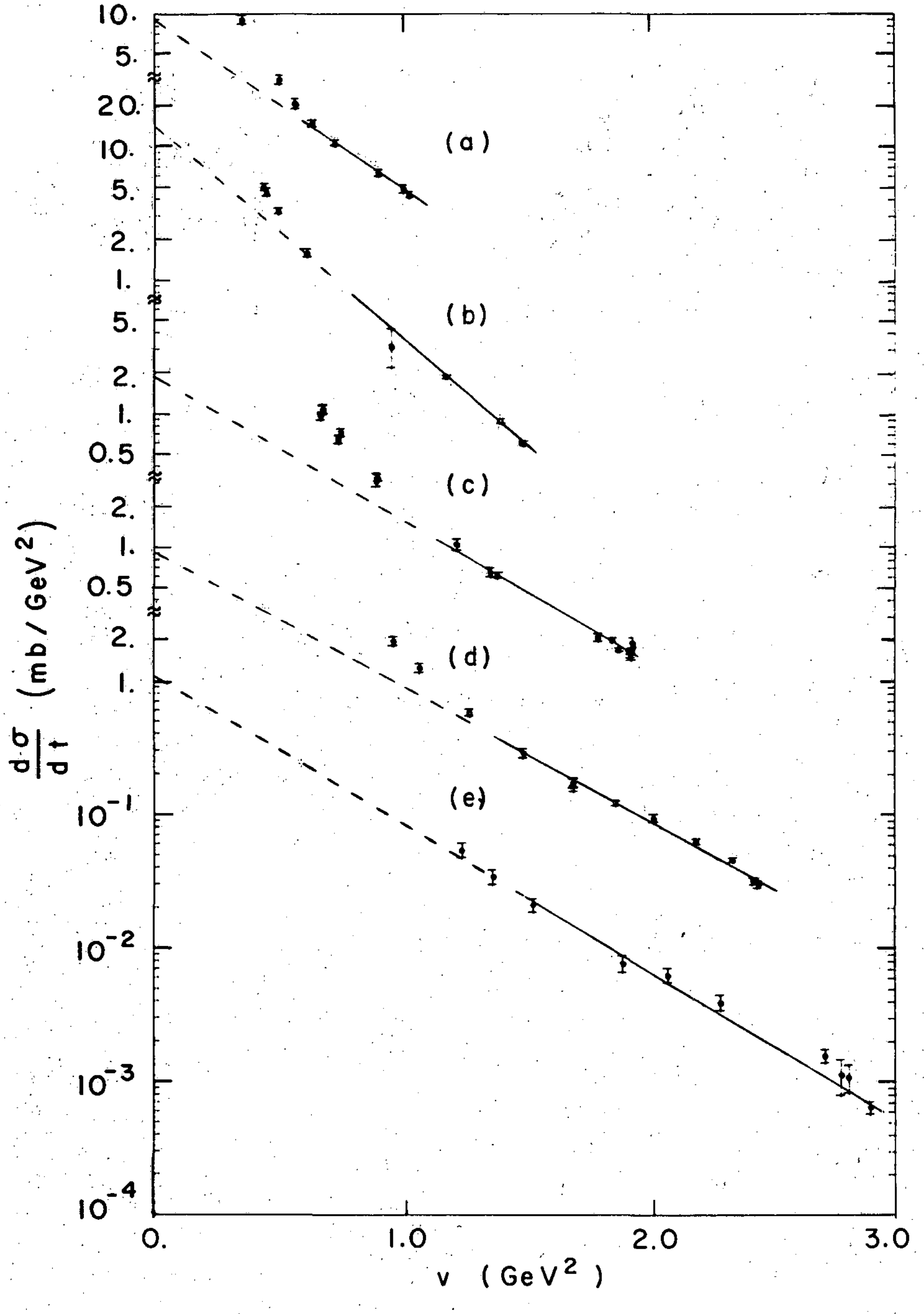

XBL677-3656

Fig. 15

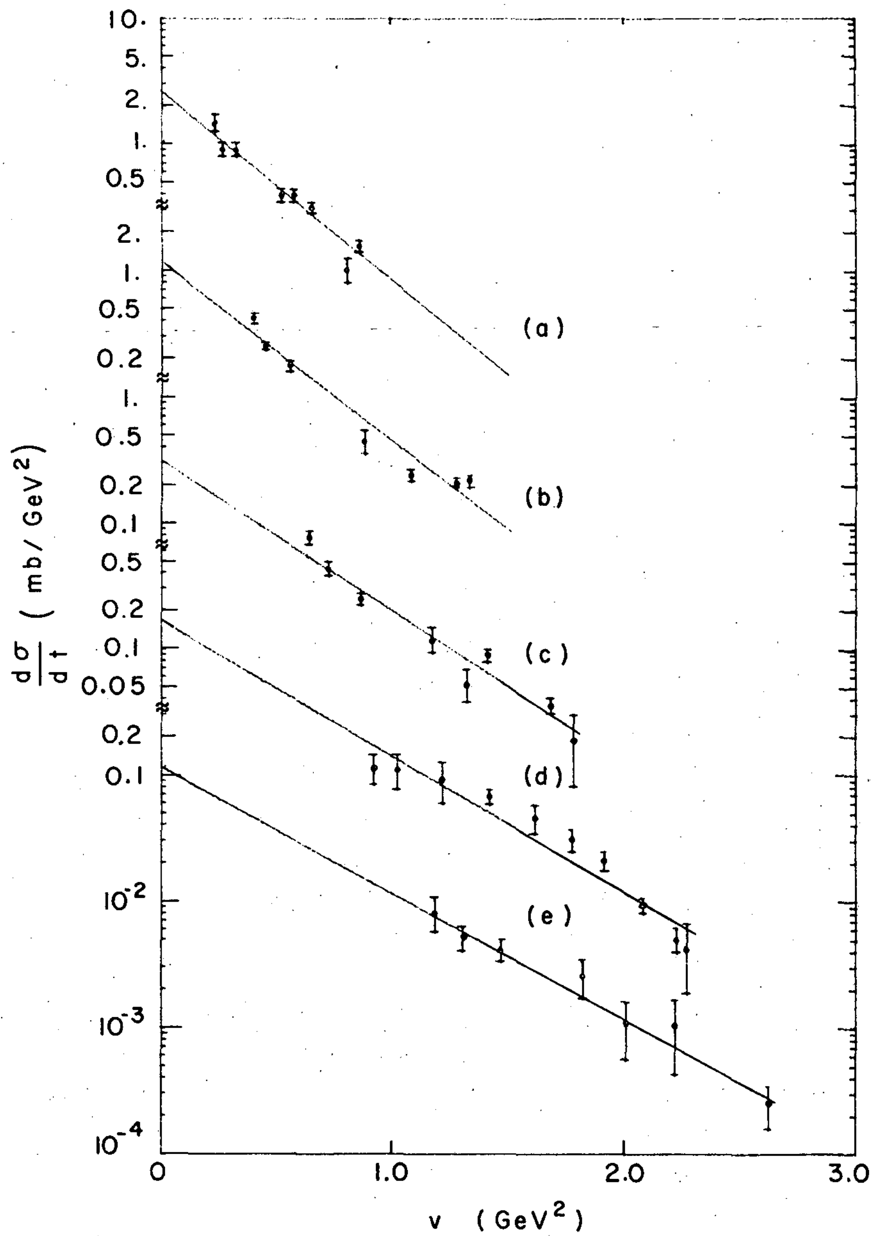

Fig. 16 XBL677-3655

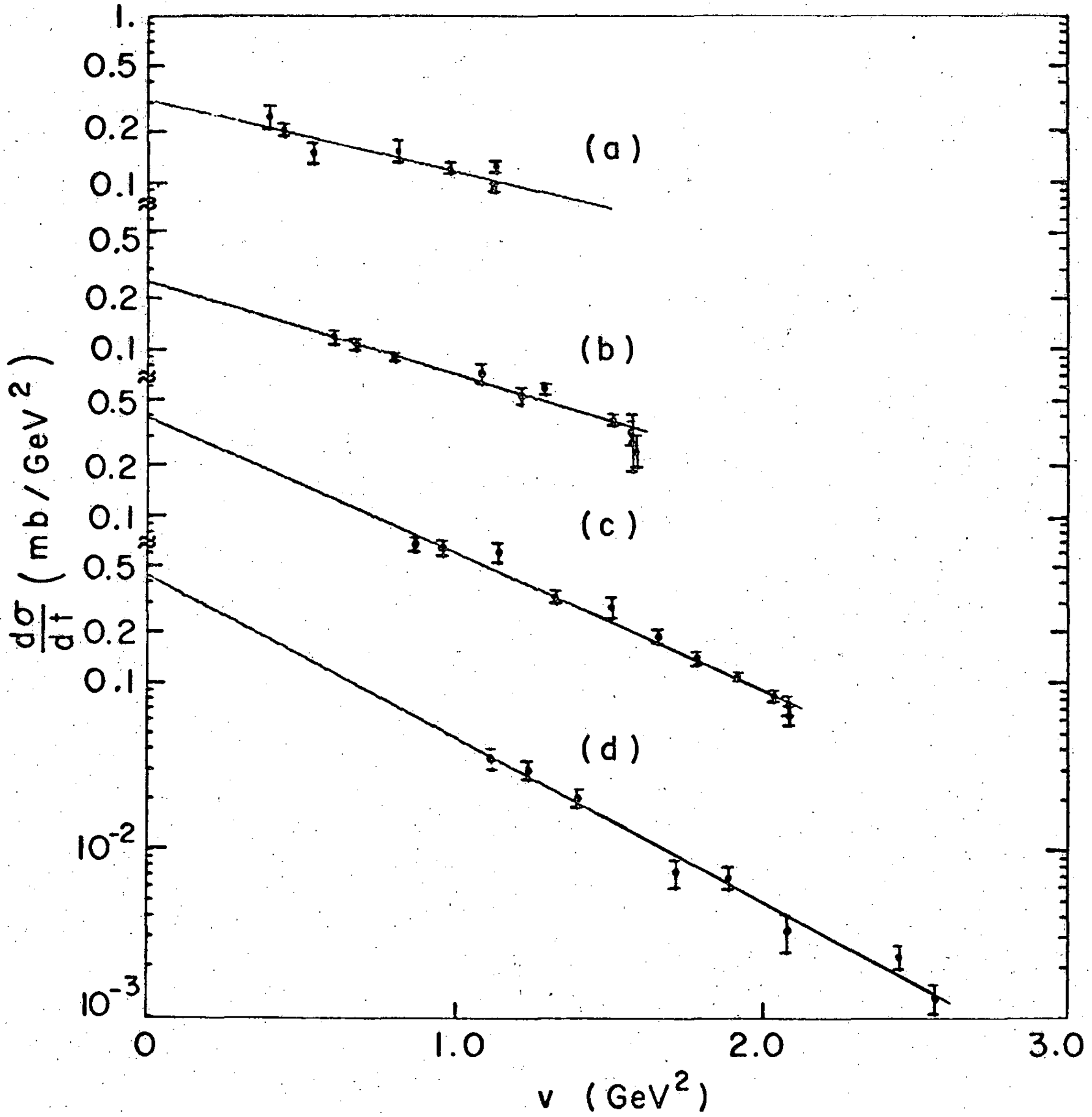

XBL677-3654

Fig. 17

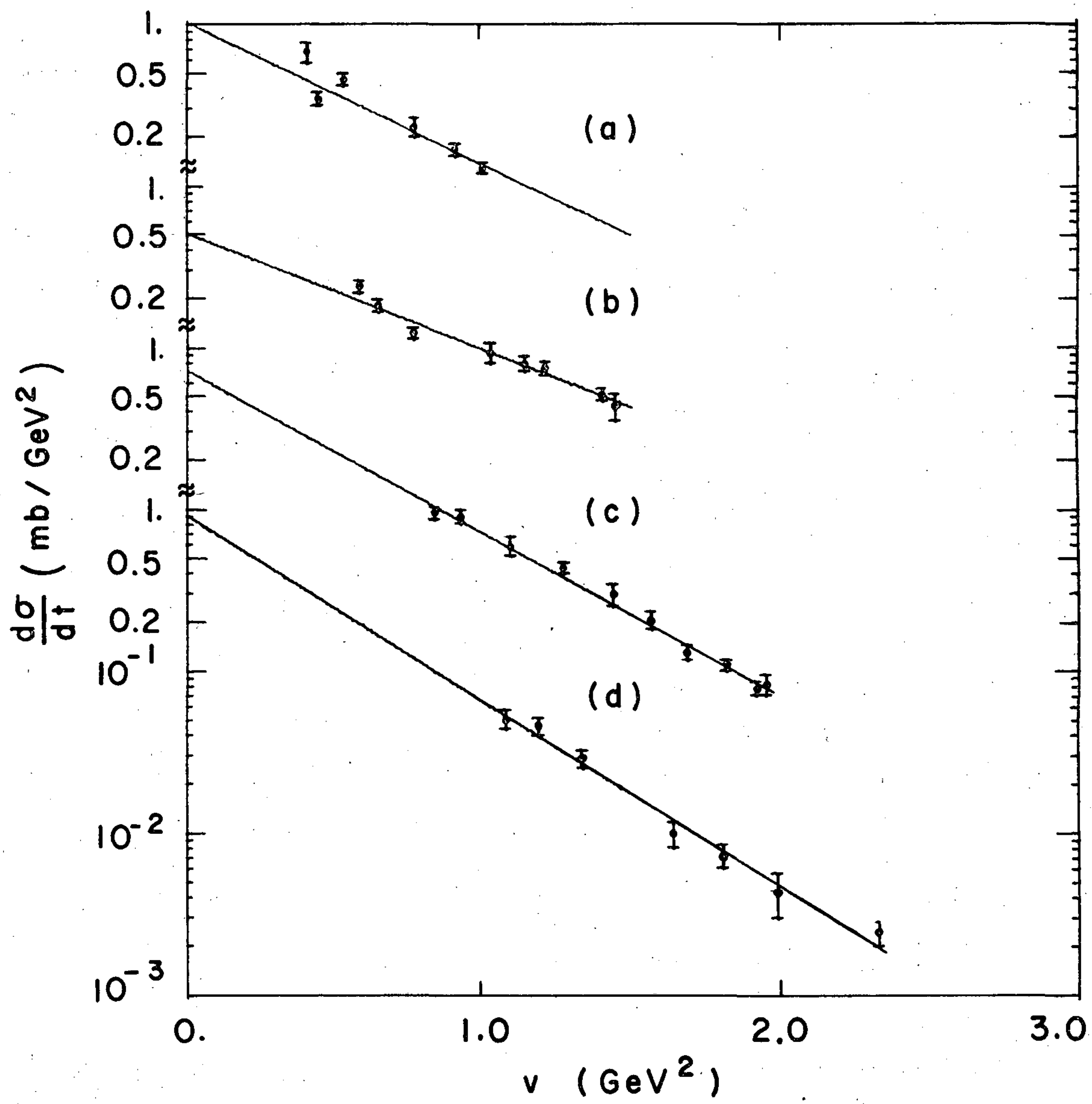

XBL 677-3653

Fig. 18

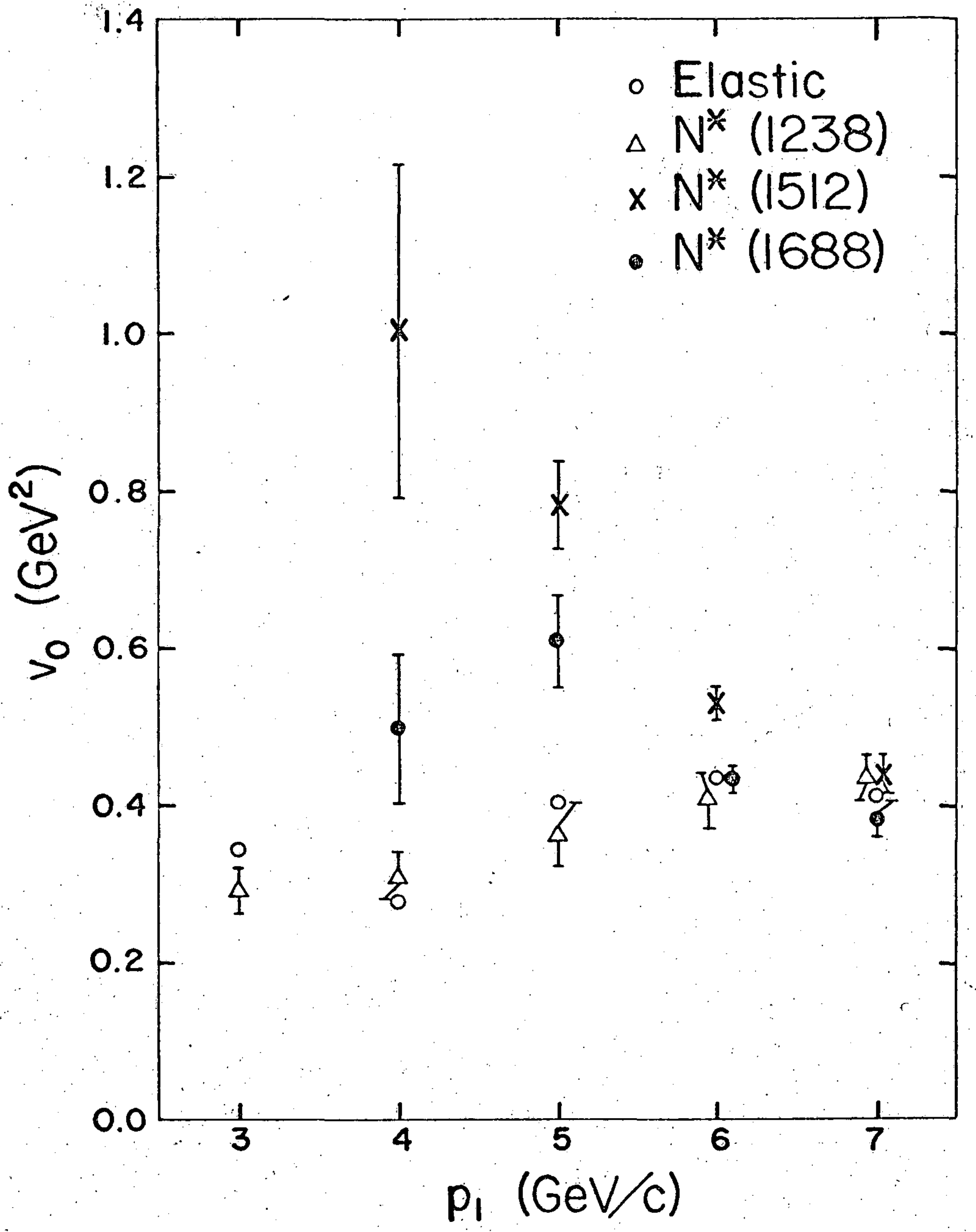

XBL 671-481

Fig. 19

UNIVERSITY OF CALIFORNIA

Lawrence Radiation Laboratory
Berkeley, California

AEC Contract No. W-7405-eng-48

March 26, 1967

ERRATA

TO: All recipients of UCRL-17763

FROM: Technical Information Division

SUBJECT: UCRL-17763, "Nucleon Isobar Production in Proton-Proton Collisions between 3 and 7 GeV/c," C. M. Ankenbrandt, A. R. Clark, B. Cork, T. Elioff, L. W. Kerth, and W. A. Wenzel, January 2, 1968.

Please correct subject report as follows:

Cover, title: Change "GeV/v" to GeV/c.

Page 15, line 20 should read: the elastic scattering region. In order to obtain the elastic-scattering---

Page 23, lines 21, 22, and 23 should read:

where $t = (\underset{\sim}{p}_1 - \underset{\sim}{p}_3)^2$

and $u = (\underset{\sim}{p} - \underset{\sim}{p}_4)^2$.

For elastic scattering, $v \equiv p_\perp^2$, $t = -2p^2(1 - \cos\theta)$, $u = -2p^2(1 + \cos\theta)$.